BRNO UNIVERSITY OF TECHNOLOGY
VYSOKÉ UČENÍ TECHNICKÉ V BRNĚ

FACULTY OF MECHANICAL ENGINEERING
FAKULTA STROJNÍHO INŽENÝRSTVÍ

INSTITUTE OF PHYSICAL ENGINEERING
ÚSTAV FYZIKÁLNÍHO INŽENÝRSTVÍ

DESIGN OF AUTOMATED SET-UP INTENDED FOR INSPECTION OF PMMA COATED SILICON WAFERS

NÁVRH AUTOMATIZOVANÉ APARATURY URČENÉ PRO INSPEKCI KŘEMÍKOVÝCH DESEK OVRSTVENÝCH PMMA

BACHELOR'S THESIS
BAKALÁŘSKÁ PRÁCE

AUTHOR — Michal Drozd
AUTOR PRÁCE

SUPERVISOR — Ing. Alexandr Knápek, Ph.D.
VEDOUCÍ PRÁCE

BRNO 2020

BRNO UNIVERSITY OF TECHNOLOGY
FACULTY OF MECHANICAL ENGINEERING

Specification Bachelor's Thesis

Department:	Institute of Physical Engineering
Student:	**Michal Drozd**
Study programme:	Applied Sciences in Engineering
Study branch:	Physical Engineering and Nanotechnology
Supervisor:	**Ing. Alexandr Knápek, Ph.D.**
Academic year:	2019/20

Pursuant to Act no. 111/1998 concerning universities and the BUT study and examination rules, you have been assigned the following topic by the institute director Bachelor's Thesis:

Design of automated set–up intended for inspection of PMMA coated silicon wafers

Concise characteristic of the task:

Student will deal with the development of experimental instrumentation designed for detection and localization of defects in the electron resist (PMMA) on silicon wafer intended for exposure within an e–beam lithography system. Within the frame of the work, custom hardware will be developed and implemented by means of existing methodology with student–created software. The work will be carried out in the laboratories of the E–Beam Lithography Group at the Institute of Scientific Instruments of the ASCR.

Goals Bachelor's Thesis:

1. To do a literary research mapping the topic and to process the current state of the research describing the basic types of defects.
2. To design the mechanical and electronic part of the set–up which will be used to implement the existing methodology achieving fully automated control using a computer.
3. To design and implement a control algorithm for detection of inhomogeneities and to verify its functionality using designed hardware.
4. To perform a set of experimental measurements and to evaluate the results. Also suggest possible adjustments or improvements for the future.

Recommended bibliography:

MATĚJKA, F. Praktická Elektronová Litografie, Brno: Ústav přístrojové techniky AV ČR, 2013. ISBN 978-80-87441-04-6.

OBERAI, A. a J. S. YUAN. Smart E-Beam for Defect Identification & Analysis in the Nanoscale Technology Nodes: Technical Perspectives. Electronics 2017, 6, p. 87.

PEERSON, I. et al. Litography defects: Reducing and managing yield killers through photo cell monitoring. Yield Management Solutions, Vol.2 Issue 3, 2000, pp. 17-24.

KOCH, Ch. a T. J. RINKE. Photolitography: Basic of Microstructuring, MicroChemicals GmbH, 1st edition 2017, pp. 58-62.

Deadline for submission Bachelor's Thesis is given by the Schedule of the Academic year 2019/20

In Brno,

L. S.

prof. RNDr. Tomáš Šikola, CSc. Director of the Institute	doc. Ing. Jaroslav Katolický, Ph.D. FME dean

Summary
During the coating the substrate with a thin layer of polymer resist several defects can to occur which could damage an exposure by electron beam lithography. The quality of the resist-coated surface prior to the exposure is also very important in terms of the final functionality of the fabricated micro device. The quality of the resist-coated surface can be measured by means of human visual inspection with a visible-light microscope. This bachelor's thesis is focused on the design and assembly of the automated set-up to do this inspection automatically.

More precisely, the designed set-up is called WaferScan and it allows to scan a silicon wafer coated with a resist layer. The wafer surface is scanned with an optical camera and the taken images are analyzed using computer to determine the location and the size of the defects and the dust particles in the resist layer. The entire device consists of two moving axes, x and y, (that allow the movement of the camera) and a control electronic circuitry. Software to control the scanning device and the image processing tool were also developed.

Abstrakt
Při ovrstvování substrátu tenkou vrstvou polymerního rezistu dochází k defektům, které mohou poškodit celou, někdy i několikadenní expozici pomocí svazku elektronů - elektronovou litografií. Kvalita nanesené vrstvy, která je potřebná k následnému deponování, je velmi důležitá z hlediska následné funkčnosti vyráběné nanostrukutry. Předběžnou kontrolu kvality naneseného resistu je možné dělat ručně pomocí světelného mikroskopu. V rámci této bakalářské práce vznikl prototyp zařízení, které tyto defekty dokáže detekovat automaticky.

Přesněji jde o rastrovací zařízení pojmenované WaferScan, umožňující skenovat křemíkovou podložku (wafer) optickou kamerou a analýzou obrazu v počítači zjistit polohu a velikost defektů a prachových částic v rezistu naneseném na waferu. Celé zařízení se skládá ze dvou pohyblivých os x a y, které umožňují pohyb kamery, a příslušené elektroniky. Součástí je také software k ovládání zařízení a zpracování obrazu.

Keywords
e-beam lithography, EBL, resist discontinuities, quality control, image processing

Klíčová slova
elektronová litografie, defekty v rezistu, kontrola kvality, zpracování obrazu

DROZD, M. *Návrh automatizované aparatury určené pro inspekci křemíkových desek ovrstvených PMMA*. Brno: Vysoké učení technické v Brně, Fakulta strojního inženýrství, 2020. 40 s. Vedoucí bakalářské práce Ing. Alexandr Knápek, Ph.D..

I hereby declare to have written this thesis on my own, under the supervision of Ing. Alexandr Knápek, Ph.D., my bachelor's thesis supervisor. I have used no other resources except those cited and mentioned in the references.

Michal Drozd

I hereby express my gratitude to my supervisor, Ing. Alexandr Knápek, Ph.D., for his time, guidance, encouragement, comments and ideas related to the thesis drafts. I owe my thanks to doc. Ing. Vladimír Kolařík, Ph.D.; Stanislav Král; Ing. Milan Matějka, Ph.D.; Bc. Jana Chlumská and all of my colleagues from the E–Beam Lithography Group at the Institute of Scientific Instruments of the Czech Academy of Sciences, for their valuable words of advice and tremendous help. I would also like to acknowledge the institutional support RVO:68081731 provided by the Czech Academy of Sciences. I give special thanks to my family for the excellent care and support I was provided during my studies.

Michal Drozd

Contents

1. Introduction

Electron beam lithography (EBL) was invented nearly sixty years ago and now it is one of the most common techniques for patterning at the sub-10 nm resolution. It has enabled the nanofabrication of structures and devices within the research field of nanotechnology and nanoscience. Demands for improvement and streamlining of lithographic processes are still growing, and therefore it is necessary to develop and improve it. Thanks to EBL, there are devices like solid-state drives, random-access memories, microprocessors or more scientific applications like quantum structures, transport mechanism studies of semiconductor interfaces or optical devices.

In the Czech Republic this technology development began at the end of the 1970s. This was preceded by a collaboration of three scientists of Brno University of Technology, Armin Delong, Vladimír Drahoš and Ladislav Zobač. In the 1950s, they constructed the first scanning electron microscope (SEM) in the then Czechoslovakia. And it was extremely successful. In 1958, it won a gold medal in the 1958 Brussels World's Fair (EXPO 58) and professors A. Delong and V. Drahoš received a state award. Based on their work Institute of Scientific Instruments of the Czechoslovak Academy of Science (ISI CSAV) was founded and granted a production license to Tesla Brno company, where over 1 100 SEM units were made. In ISI CSAV, began to work on new projects, one of which beeing the construction of an electron beam lithography system Tesla BS600 in 1977–1987. It has been continuously modernized until now. The recording resolution (beam positioning) is of 50 nm and this lithograph has one big advantage – the apertures form a rectangular beam, which is not entirely common in industrially produced lithographs and it is very useful in exposure time optimization. In 2013, lithograph Vistec EBPG 5000+ HR (fig. 2.1) was purchased by this institute, with working voltage of up to 100 keV and with a Gaussian electron beam. Thanks to that, new opportunities emerged.

In the first part of this bachelor's thesis, the Chapter 2 represents a general overview of the electron beam lithography technique from the history, offers an explanation of the electron beam lithography system, the electron beam lithography process, including spin-coating, an explanation of defects which can appear in a resist layer and how they are detected at the Institute of Scientific Instruments of the Czech Academy of Science (ISI CAS). It is made manually under a visible-light microscope (see fig. 1.1), the scientist measures it in rows at 3 mm intervals in a controlled area of about 50 mm × 50 mm. At each place where a defect is found, its dimensions are measured and written in a chart. Thus, it takes a lot of time, dozens of minutes per one wafer. Moreover, there are possible human errors due to inattention or oversight as well as the fact that wafer is only loosely placed on the microscope positioning table.

Thanks to that, an idea arose to automate the inspection process of the spin-coated wafer. So the purpose of this bachelor's thesis is to design and assemble a measurement set-up introduced in the Chapter 3 which would prove to detect all defects in a resist layer, measure them and send their pictures to a database. It entails a hardware implementation which consists of an engineering and an electrotechnical part. The engineering solution requires a precise design in a clean room, with a sufficiently rigid construction and a range of motion sufficient for measured wafers. The electrotechnical solution requires to work with a microcontroller board, to choose the right motors and optical devices that will allow to take pictures with sufficient resolution. But it also involves software development to control the set up and to process the taken images, using an appropriate algorithm.

Figure 1.1: The scientist inspects defects on the wafer surface using a visible-light microscope

With the assembled set up and the programmed software a set of measurements was made which is explained in the Section 3.3. And the Section 3.4 mentions possible future improvements following the findings of the measurement.

2. Theoretical Part

2.1. Historical background of E-beam Lithography

Lithography is a process of transferring patterns to the surface of a substrate. Lithography was invented by Alois Senefelder in 1796. He used it to print dramatic pieces and notes. The old lithography process may be summed up as follows. An image is drawn to a plate with oily ink or lithographic chalk which fills the pores of the stone. Then the thin layer of water does not fill the painted places and the printing ink fills the places where there is no water. The big advantage is that a single stone can yield an almost unlimited number of copies [24].

As the time goes, people wanted to make lithographic structures smaller and smaller, so they started to use light and photosensitive materials. This is called optical lithography, a substrate is coated with a photosensitive material (photoresist) which is then exposed by light and etched using a chemical substance. The minimal resolution of this technology is limited by the used lens system and the wavelength of the used light. A higher numerical aperture NA of the lens system and a shorter wavelength λ are used; a higher resolution R of the optical lithography is practicable, it is given by the condition 2.1, where k_1 is a constant dependent on the resist material, the process, and the image formation technologies [19] [20].

$$R = \frac{k_1 \lambda}{\mathrm{NA}} \tag{2.1}$$

A big change came in the 1960s when researchers at the Bell Laboratories converted a scanning electron microscope (SEM) into an e-beam writer. This gave rise to the first e-beam lithography (EBL) system. Electrons, like photons, possess particle and wave properties. However, their wavelength is on the order of a few tenths of an angstrom and their resolutions are not limited by diffraction. So, it is possible to make much smaller structures capable of submicrometer pattern definition and it is currently used by many companies to manufacture specialty, high-resolution devices. Although EBL has not had as much significance as optical lithography in mass fabrication, due to the slow writing of milions of pixels, EBL can be used in the fabrication of photomasks that are used with projection photolithography systems [26]. Other applications of EBL are research and development in the area of integrated circuits and direct creating of advanced prototypes in the nanoscale range.

In the Institute of Scientific Instruments of the Czech Academy of Science (ISI CAS), by EBL, diffractive optically variable image devices (DOVIDs), micro-sensors, calibration specimens as well as electrochemical and biological sensors are made. Worldwide, EBL is for example necessary in the computer chips fabrication.

2.2. Electron beam lithography system

The electron beam lithography system (a lithographer, see fig. 2.1) is similar to SEM. However, it is able to expose much bigger patterns with more precision moves with a sample stage. An architectural example of the lithographer is shown in fig. 2.2. The electron optical column has an electron beam source on the top – an electron gun, in most cases a thermal emission cathode or a thermally assisted field emission cathode. Follows the

Figure 2.1: An example of electron beam lithography set up, VISTEC EBPG5000+HR at ISI CAS [15]

beam shaping optics, transferring the first aperture image into the second aperture. And at the end of the column, there are deflectors, necessary for scanning with an electron beam, and a set of focusing and objective lenses. It is necessary to ensure better throughput, accuracy, and resolution of the system. The column should be kept at a high vacuum of 10^{-6} Pa to 10^{-8} Pa.

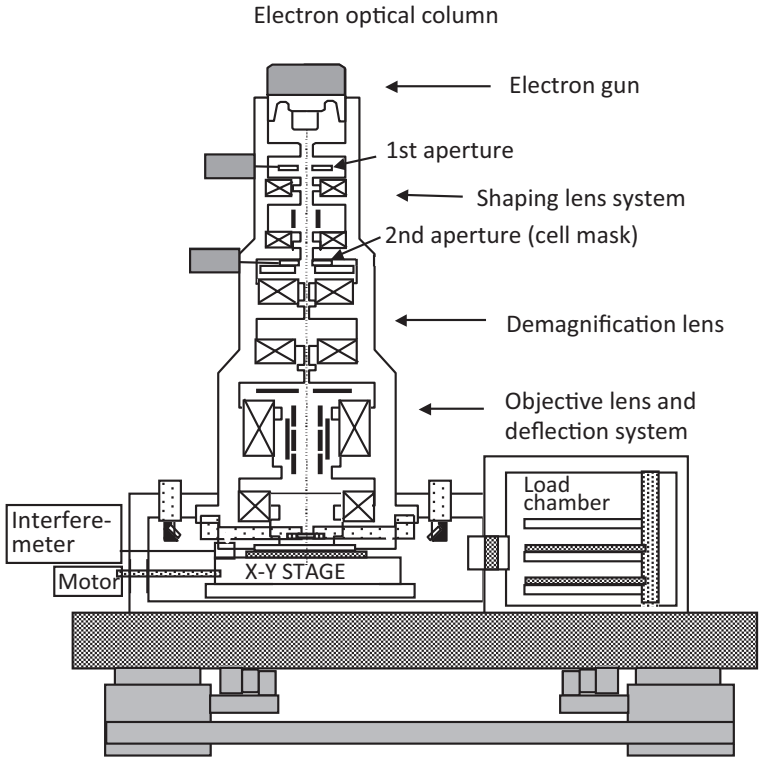

Figure 2.2: An architecture example of an electron beam lithography set-up [23]

The mechanical system consists of a wafer stage and a loading system. The stage moves inside the chamber in the vacuum under the control of a laser interferometer, which allows the high precision movement. It is because the scanning field size of deflectors is generally smaller than a desired pattern. It is smaller than a few millimeters due to the distortion limit and optical aberrations. The system also includes a workstation which controls the overall system and of software which handles the data preparation, the exposure control and the overall diagnosis and maintenance [15] [23].

2.3. Preparation of the resist layer

The fist standard step of the electron beam lithography process is spin coating. The objective of this step is to obtain a uniform, adherent, defect-free polymeric film over the entire substrate. A few millilitres of the liquid polymer is dispensed in the middle of the substrate with a pipette or a resist supply and then spread out by slow spin at a rotational velocity of approx. 500 min^{-1}. After that, the spin speed is increased to 2000–4000 min^{-1} [4]. Figure 2.3 illustrates an example of a spin coater. For a given resist thickness t, which is a function of the polymer concentration C, the molecular weight which is represented by the intrinsic viscosity η, and the rotating speed ω, the formula looks like as follows [26]

$$t = \frac{KC^{\beta}\eta^{\gamma}}{\omega^{\alpha}} \tag{2.2}$$

where K is an overall constant and β, γ and α are constants of relevant variables.

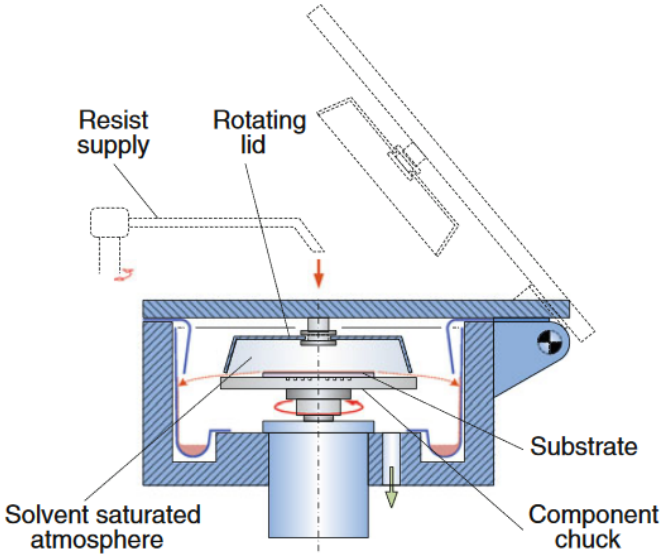

Figure 2.3: Spin coating [4]

While formula 2.2 allows us to predict the thickness t of the film, it does not predict the quality of the film that will be obtained. These properties are determined primarily by the spinning solvent, its volatility and polymer-solvent interaction. Solvents, which are highly volatile, evaporate rapidly, they have a high increase in viscosity, thereby preventing the film from forming a uniform thickness over the whole substrate. Thin resists are preferred for better resolution, but are prone to particle defects and the pinhole density rapidly increases with a lower resist thickness [3].

After spin coating and air-drying, the polymer film contains 1 % to 3 % of the residual solvent. In order to remove it, a pre-baking step prior to the exposure itself is necessary. If the pre-baking schedule is followed rigorously, this step does not generally introduce any problems in subsequent processing, unless of course, the baking equipment itself is contaminated. In that case, defects may be generated. Once particles contact a resist surface prior or during the pre-baking, they are almost impossible to remove and it will cause opaque spots or pinholes after exposure and development [26].

2.3.1. Wafer – the typical substrate for EBL

A typical substrate for EBL is a silicon wafer, which is a thin slice of a single crystal silicon ingot. The crystal orientation is defined by the Miller index and, for easy recognition, the wafer has flats, cut into one or more sides indicating the crystallographic planes. At ISI CAS, wafers with the Miller index (100) are often used because to split more patterns from one wafer, it is easier to break them in horizontal and vertical rows along the crystallographic planes. We will be interested in sizes 4" and 6" which are the most commonly used in scientific applications. They correspond to the diameter of 100 mm and 150 mm respectively. Thickness of the wafer is around 0.6 mm.

2.3.2. Chemical properties of the electron beam resist

Resists can be divided into several groups, to organic and inorganic, or to positive tone and negative tone. In case of the positive resist, after the exposure, it is dissolved during development, the negative resist is developed in places, where it was not exposed.

Soon after, a commonly used, organic poly (methyl methacrylate) (PMMA) was found to be ideal for an electron beam lithography. It behaves as a positive tone resist under EBL but also X-rays and Deep UV radiation. The exposure induces the scission of the chain of methacrylate monomers, so the main process consists of the break of the main chain, but other scission possibilities may also occur (to see fig. 2.4) [5][22].

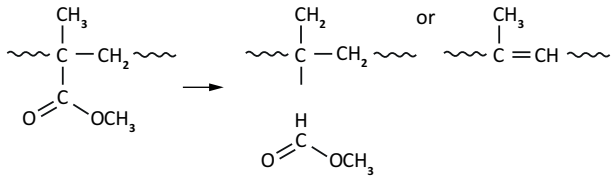

Figure 2.4: Schematic diagram for one repeat unit of PMMA and one of its generic reaction path [5]

2.4. Types of defects in the resist layer

During a resist layer preparation, various defects may occur. They are caused by impurities on the wafer, such as dust particles, fibers or micro-bubbles in the resist mixture, or they are caused by poor centering of the wafer on a spin coater. Defects in the resist can be divided in two groups. Defects caused by impurities stacked to the resist layer during the coating or the prebaking. Or defects caused by the processing technology of the resist layer preparation [10].

2.4.1. Defects caused by impurities

Although the preparation of resist is performed under laminar flow, there is still a chance that impurity occurs in the prepared layer. It depends on the class of cleanroom. ISO standards employ units of particles per cubic meter (table. 2.1) [3]. In ISI CAS, there are clean rooms with ISO class standard 3 and 4. And the preparation of resist layer is done under a flowbox. The use of a N_2 pistol immediately before the resist coating also helps blow away a certain fraction of the particles from the substrate surface. But still, some impurities get to the resist layer during the spin coating or the baking.

Table 2.1: ISO standard of particle cleanliness classes ($/m^3$)

	0.1 µm	0.2 µm	0.3 µm	0.5 µm	1 µm	5 µm
ISO class 1	10	2				
ISO class 2	100	24	10	4		
ISO class 3	1 000	237	102	35		
ISO class 4	10 000	2 370	1 020	352	83	
ISO class 5	100 000	23 700	10 200	3 520	832	29

If a dust particle or a fiber falls on the wafer surface during spin coating, it stays in the resist layer and forms a "Comet". Thus it makes a thickness difference in the resist from the center of the particle to the edge of the wafer. Other impurities are small resist flakes that stick to the layer and get permanently attached to the surface due to the baking [13].

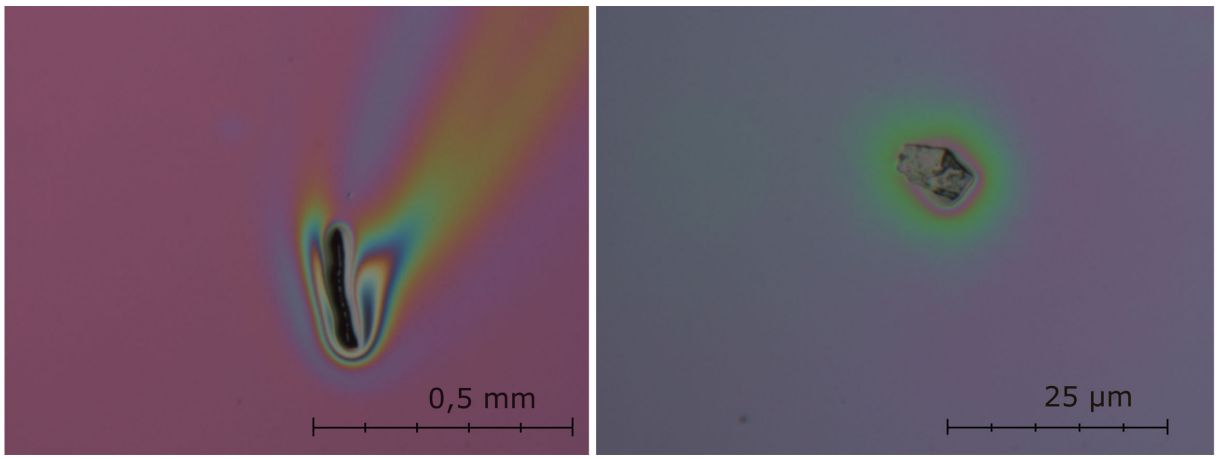

Figure 2.5: Fiber creating a cornet (left), a resist flake baked in the layer (right)

2.4.2. Defects caused by the processing technology

Besides impurities, defects can form due to errors in the process technology. Defects may be generated during the spin coating operation in which case they are generally observed to be distributed radially. Among them are bubbles in the resist mixture, created by an incorporation of air bubbles into the liquid resist during transportation of the resist bottle (e.g. in the clean room), or by refilling resist into another container or by pipetting. The micro bubbles are created after the subsequent coating on the wafer. There are small spots in the resist layer with a huge thickness difference, which causes problems during

the exposure, such as cracks in the resist layer around these spots. This can be prevented by degassing the mixture in a desiccator, by slowly pouring the resist mixture on the wafer, or by a delay, preventing the moving of the resist in the container.

Another issue in this category of defects occurs due to an insufficient centering of the wafer on the spin coater, either by a poorly levelled spin coater or by an improper choice of the spin coating parameters. This type of defect is difficult to see in a microscope because of the small field of view. It is much easier seen by a naked eye, or by an optical instrument with a larger field of view than that of a microscope.

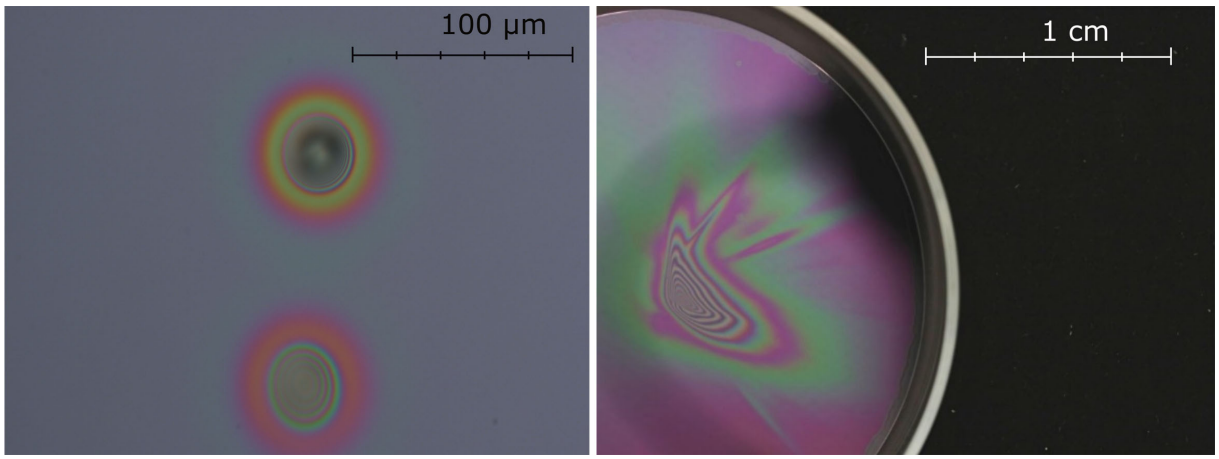

Figure 2.6: Micro bubbles (left), an inhomogeneity all over the wafer (right)

2.5. Inspection of the resist layer

The deposition by an electron beam to the coated substrate could take long time, in some cases a few days. Thus it is necessary, before the exposure itself, to be sure that the resist does not contain defects which could affect the resultant pattern. Also, the quality of the resist-coating is very important in terms of the final functionality of the fabricated micro device. At ISI CAS, the inhomogeneities in the resist larger than 10–15 μm are problematic in the EBL process. For the detection of such size defects a visible-light microscope with 5X objective is used. The scientist manually moves the microscope table in x and y axes to control important central places in the resist layer of the wafer, it is about 50 mm $\times$ 50 mm. It is done in rows of 3 mm intervals. When a defect is found, it is written to a defect map in the wafer diagram; its size, position, and its type (see fig. 2.7). Coated wafers are then stored with its identification number and when a wafer is needed to be exposed, a suitable one is chosen according to the wafer's documentation.

2.6. Exposure

When a wafer surface is coated with a radiation-sensitive polymeric material, an electron beam can be used to expose the pattern. It can be focused to a few nanometers in diameter. When it enters the resist, it loses energy via elastic and inelastic collisions and the resist changes its chemical properties resulting in the irradiated regions having different solubility in a particular solvent or developer than the non-irradiated regions. The realization of the required dose D [μC.cm^2] is obtained as in the formula 2.3.

$$D = J\tau \tag{2.3}$$

where J is the current density of the e-beam and τ is the time of exposure of one dose. Current density is very hard to change in a short time, so the dose is set by τ [14].

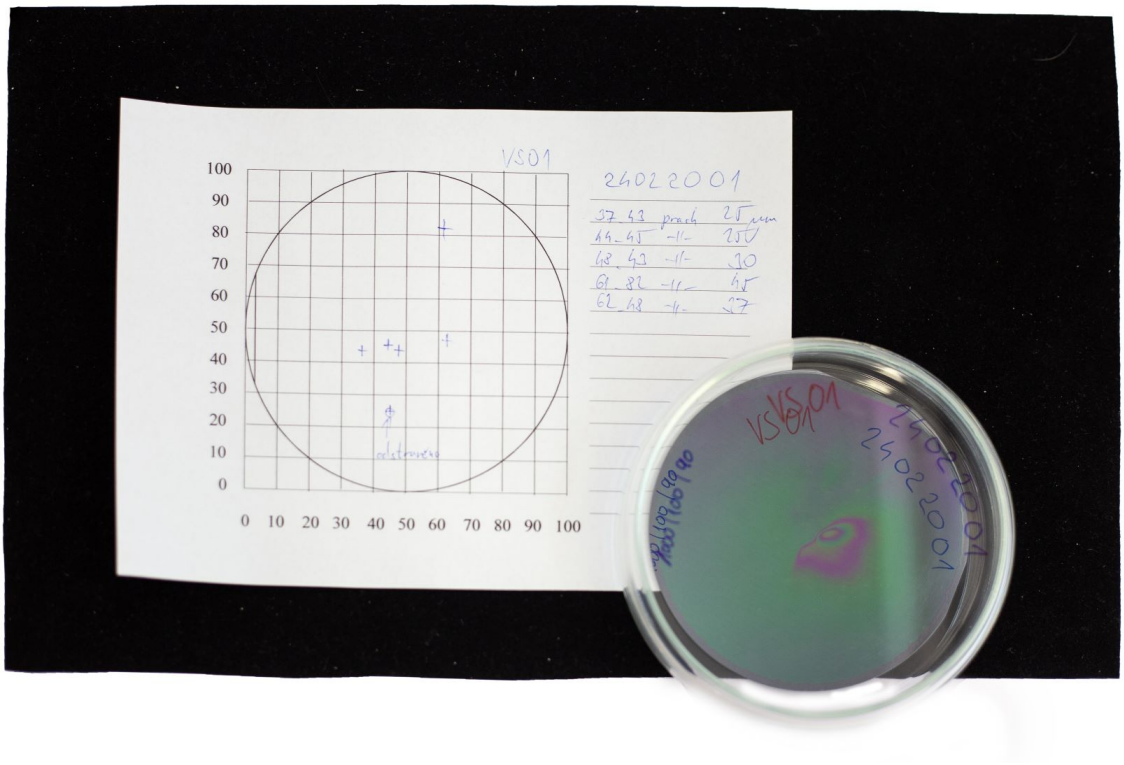

Figure 2.7: Measurement of the size and position of defects in the resist in a wafer surface

The contrast γ describes how abrupt the dependence of the relative thickness w is on the dose. It is determined from the linear slope of the sensitivity curves of the resist in fig 2.8 and it is given by 2.4 for the positive resist and by 2.5 for the negative resist.

$$\gamma = \frac{1}{\log D_i^p - \log D_o^p} = \left[\log \frac{D_i^p}{D_o^p}\right]^{-1} \tag{2.4}$$

$$\gamma = \frac{1}{\log D_o^n - \log D_i^n} = \left[\log \frac{D_o^n}{D_i^n}\right]^{-1} \tag{2.5}$$

where D_i is the dose of complete exposure or full thickness exposure and D_o is the dose that causes no resist dissolution or no remaining thickness.

Electron beams are broadened in materials as a result of electron scattering. The effect of these scattering phenomena on the resulting exposed image is called the proximity effect. The most concise model for the classification and nature of this effect is the modulation transfer function (MTF) [14]:

$$M = \frac{1}{1+\eta}\left[exp\left(-\frac{\pi^2\alpha^2}{p^2}\right) + \eta\, exp\left(-\frac{\pi^2\beta^2}{p^2}\right)\right] \tag{2.6}$$

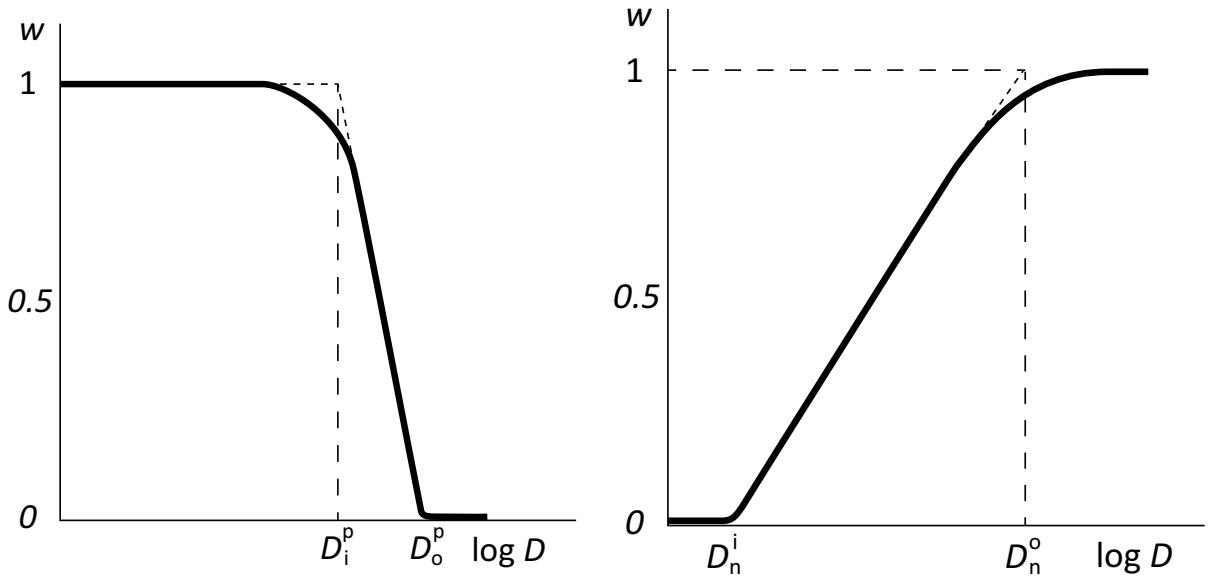

(a) (b)

Figure 2.8: Typical sensitivity curve of (a) positive and (b) negative polymer resist [14]

Where coefficient α characterizes forward-scattered electrons, coefficient β characterizes backscattered-electrons, η is the ratio of the backscattered to the forward-scattered electron energy, and p is the spatial period. MTF can be determined either by plain measurements or by using a Monte Carlo electron trajectory simulator (fig. 2.9), where you can see a simulation of electron scattering in coated PMMA on a wafer at different accelerating voltages.

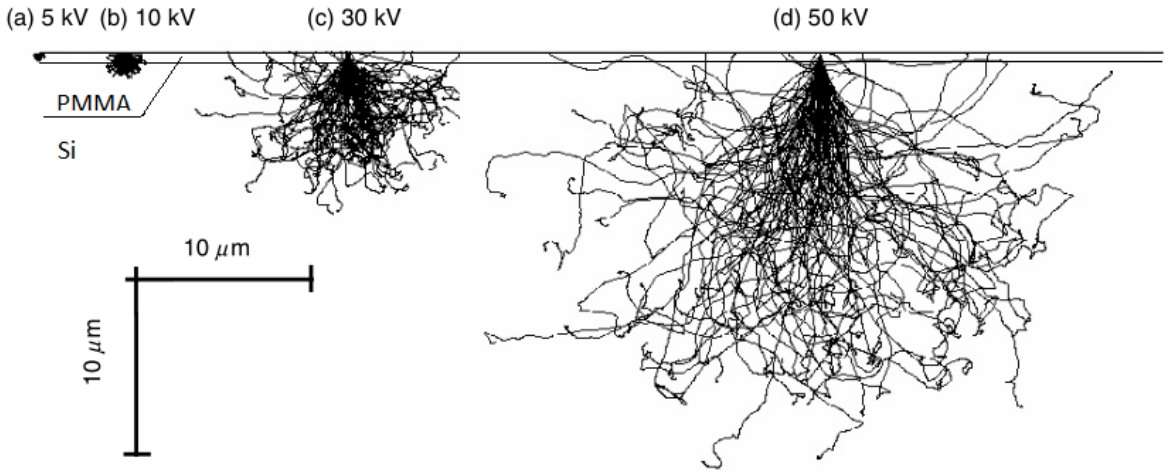

Figure 2.9: Monte Carlo simulation of electron scattering in a PMMA resist on a Si substrate at a) 5 kV, b) 10 kV, c) 30kV and d) 50kV [23]

Any particle that lands on the resist or any other undue defect prior to exposure will shield the film underneath the particle from the exposing radiation and give rise to opaque spots in the case of positive resist, or pinholes in the case of negative resists. Particulate contamination is especially troublesome with electron beam and ion beam systems where the probability of a particle landing on a substrate is increased relative to other techniques because of the much longer exposure times involved.

2.7. Development of the exposed pattern

When the latent image has been formed in the resist layer by exposure, it can be developed to produce the final three-dimensional relief image. This is the most complex step of the EBL process and has the greatest influence on the pattern quality. There are two types, a liquid development (bath) and a dry development (plasma). The liquid development is further subdivided into spray and immersion. The spray development generally gives better pattern uniformity and reproducibility. For the liquid development, tanks are used, ideally the quart vessels with a heating and temperature control. They are filled with water and chemicals. The exposed wafer is immersed in the liquid for a required time and then transferred to similar tanks for rinsing. Spray tools handle a rotating cassette and the liquid is sprayed from stationary nozzles. After the first spraying, the process can continue with different chemicals in the same vessel. The advantages are lower liquid volumes and fresh mixing of chemicals [3].

3. Measurements and Results

In Fig. 3.1, you can see a measurement set-up called WaferScan. It is designed to make raster moves over the wafer surface by degrees with a camera and to process the taken images in a laptop during and after the scanning process. It consists of a hardware implementation and software development which are described in subsequent sections 3.1 and 3.2.

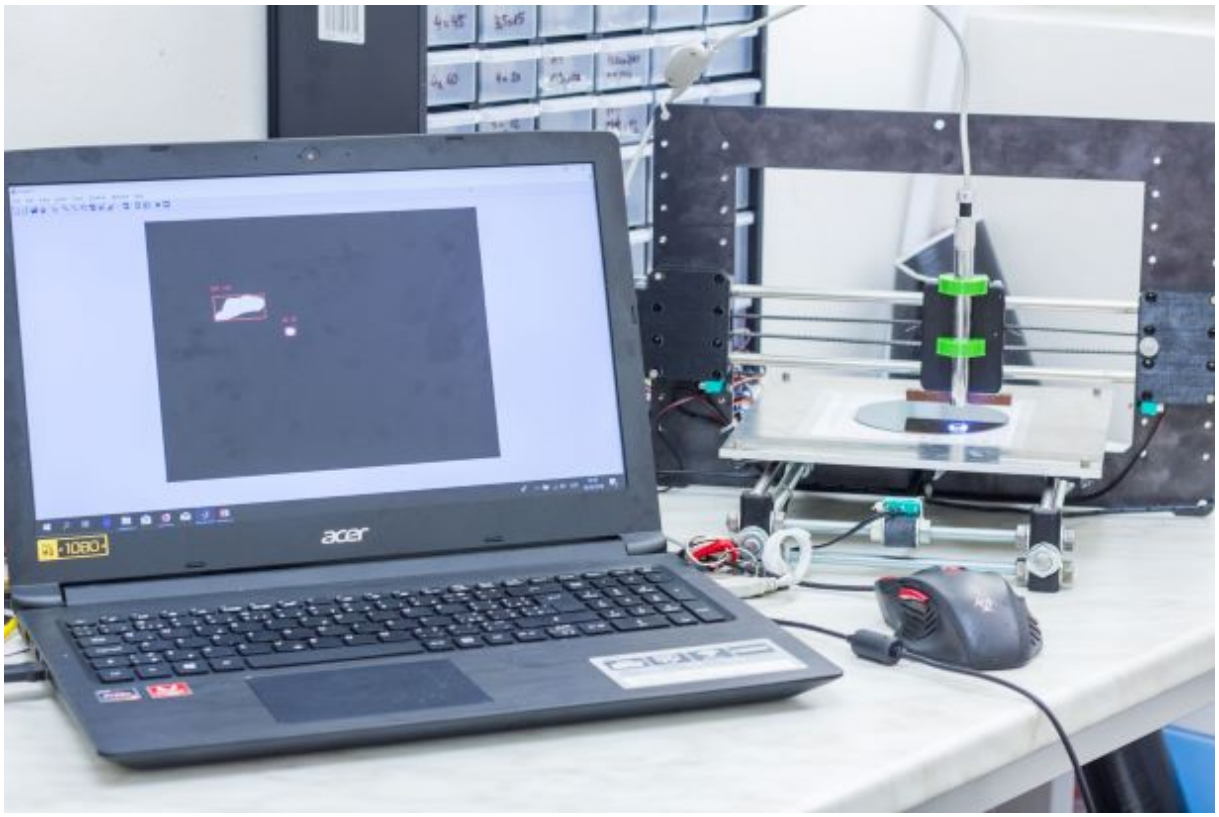

Figure 3.1: Measurement set-up

3.1. Hardware implementation

3.1.1. Engineering solution

The mechanical system is originally adapted from a 3D printer Prusa i3 MK2 with precise stepper motors and a control board mini-RAMBo. The first motor moves with a filament extruder in the x axis and the second motor moves with a stage table in the y axis, the steps corresponding to 20 µm. The filament extruder holder as well as the stage table are connected to a timing pulley of the motor with a timing belt.

In the measurement set up application (WaferScan), the same XY movement system was used (detail picture in appendix B). Just the filament extruder holder was adapted to hold the camera. To create this part, 3D printing was used. The Mini-RAMBo control board was replaced by more user friendly board Arduino UNO® (described in the next subsection 3.1.2). Moreover, the stage table was adapted to hold the wafer in a fixed position (Fig. 3.2). It is a stainless-steel plate with three screws and a stripe of flexible

sheet metal to hold the wafer in a fixed position. The position of screws is adaptive, depends on the wafer size – 4" or 6". To the stage table, a calibration sample is stuck as well comprising a 1 cm × 1 cm piece of wafer, with a cross-structure etched in its surface to preserve the xy coordinate system.

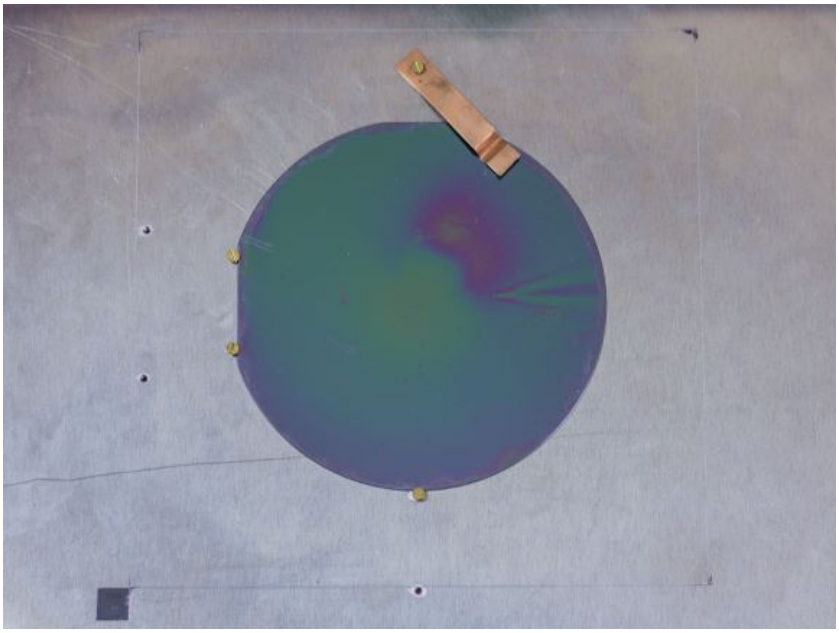

Figure 3.2: Design solution of the wafer holder, in the lower left corner you can see the sample with the calibration mark

3.1.2. Electronics

Arduino UNO®, a control board, is the main electronic part of the measurement set up. It is based on the ATmega328P microchip and can be powered by a USB (5 V) or by a 12 V DC power supply. The board has 6 analog input pins, and 14 digital I/O pins and its behavior, including whether it acts as an input or as an output, is controllable by a user at run time. The 6 pins can provide a PWM output, for example, which is useful for controlling stepper motors. A program was developed and loaded into the board itself. It is responsible for a USB communication between the WaferScan software in the laptop and the XY movement system.

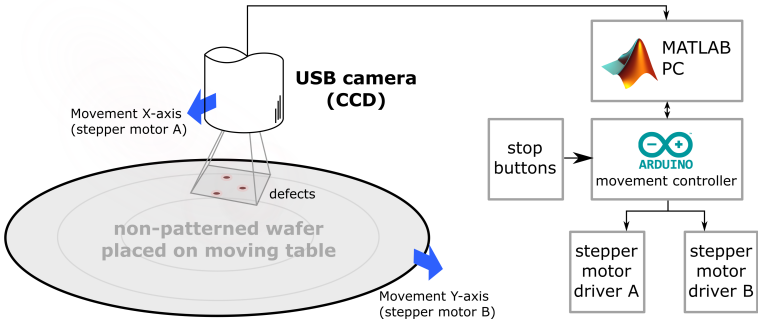

Figure 3.3: Measurement set-up diagram [10]

The Arduino interprets received commands and forwards them to EasyDrivers expansion boards (which you can see in the Fig. 3.4, right) which control the relevant motors and supply them through 12 V DC. The Arduino also generates a response back to the laptop when a relevant command is made.

The Arduino is also responsible for the control of the edges of the axes. It is done by limit switches, installed at each of the edges of the axes. When the edge is unintentionally reached, the limit switch is pressed and a command to turn off the power supply to the motors is sent to EasyDrivers. For security reasons, it is also possible to do this operation using a button with a square sign (Fig. 3.4, top). There are more options to turn on the power supply again – using the button with a triangle sign or resetting the Arduino board using the button with an arrow sign. A self-designed printed circuit board was made (Fig. 3.4, top) to form the electrical connection between individual parts, to distribute the power supply to all boards, and to allow to control the device with those buttons.

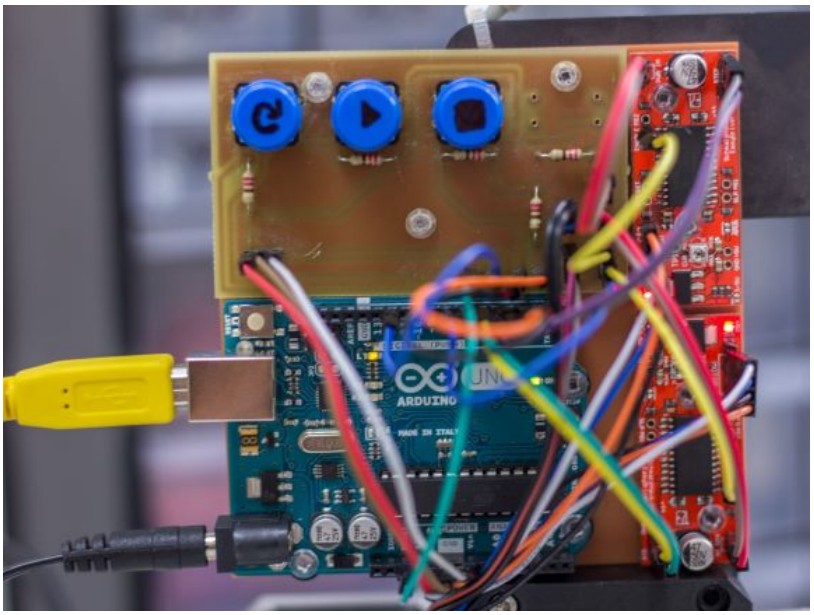

Figure 3.4: Electronics of the measurement set-up, the self-designed printed circuit board (top), Arduino UNO (bottom), and EasyDrivers (right)

Camera

The camera (Fig. 3.1.2) is based on a classical color CMOS sencor working at a resolution of 1.3 megapixels, allowing to obtain 15 screens per second with the resolution of 1280 × 1024 pixels over the USB 2.0. The camera is equipped with a white LED lighting whose intensity can be controlled manually. It is set to a maximum intensity for a lower noise and a higher shutter speed. At the minimum working distance of 7.5 mm, the field of vision is 1.36 mm × 1.02 mm.

3.2. Software solution

The WaferScan software is implemented using a Matlab graphic user interface (GUIDE®). In many cases, the official MathWorks – Matlab Support site was used.

When the software turns on, a plot with a wafer outline can be seen (1) in the main window (Fig. 3.5) which changes with a selected wafer size (6). By clicking the icon (2), the camera goes above the last position of the calibration mark (see Fig. 3.2). When the last position is wrong, it is be set it manually (3) – the power supply to motors is turned off and the individual axes can be moved manually so that the center of the field of view is directly above the center of the calibration cross. Then it is possible to calibrate the position of the camera automatically to have the calibration mark move exactly in the middle of the field of vision (4). Then, the user writes down the set and the number designation of the wafer (5). And then the zone of the inspected area – the position of its lower left corner and its size (7). It is subsequently displayed in (1) by a red rectangle. After this the raster scanning can begin by clicking the Run! icon (8). By setting coordinates in millimeters in the boxes (9), it is possible to move the camera to the exact position above the wafer. By opening the preview (10), a separate window is opened with a live view of the camera.

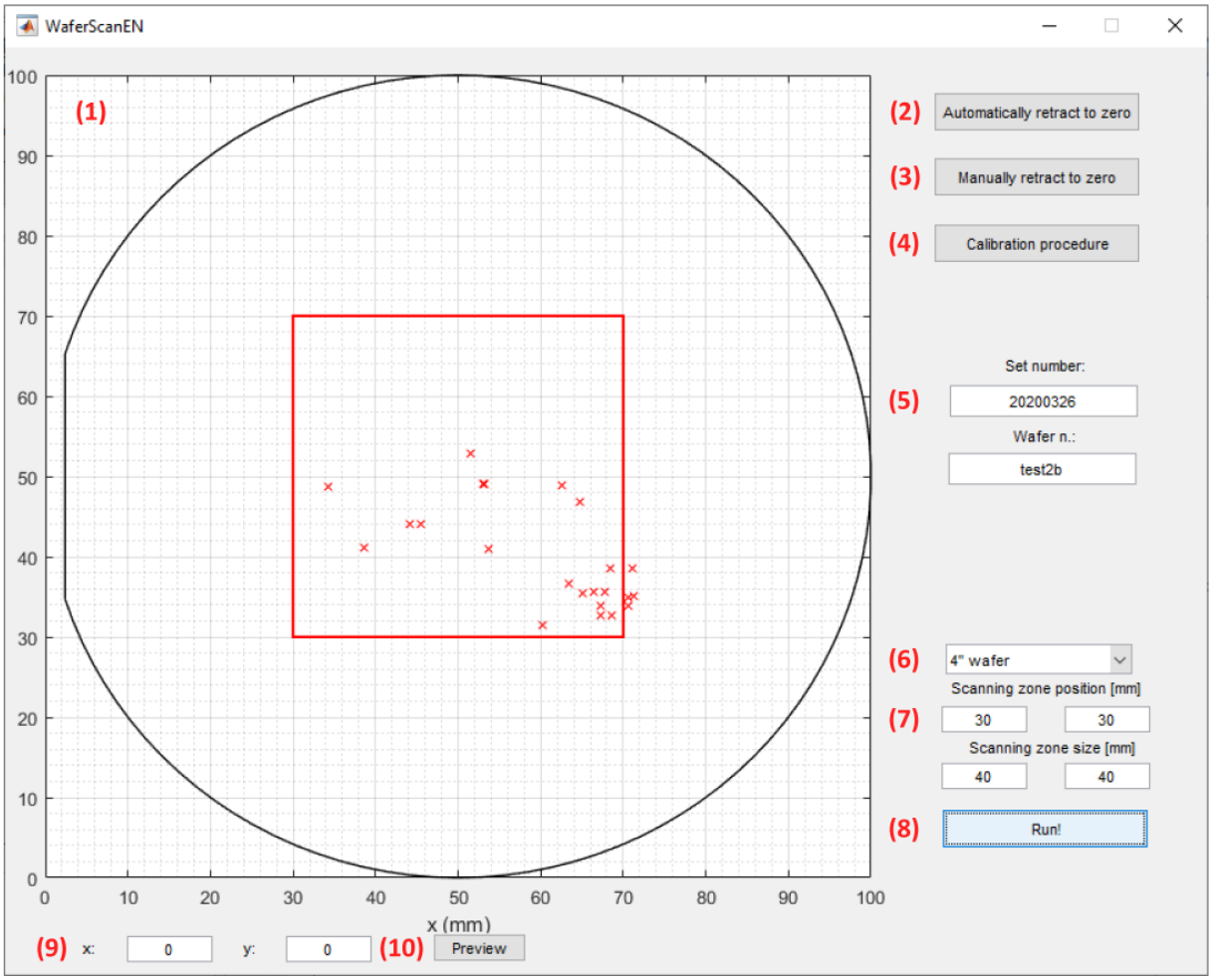

Figure 3.5: WaferScan software

3.2.1. Scanning algorithm

The main algorithm (see the flowchart 3.6) consists of a few simple steps. In the beginning, the last position of the calibration mark is located. After an automatic calibration described in the subchapter 3.2.3, a new coordinate system is set. The new system of coordinates is then used for determining the positions of any defect found during the scanning process over the surface of the selected measurement zone of the wafer. The process follows a simple scanning procedure along a zig-zag trajectory, which means that when an image is obtained, the camera moves to another field of view until the whole surface is mapped (see fig 3.7). To avoid errors in a edge of the images overlaps 0.04 mm of particular fields of view are set.

At the end of the scanning process, the software saves a "defect map", where the places appropriate to deposition (see Fig 3.5 number (1)) are clearly seen. The list of defects and their parameters is also saved. The particular images are saved continually for a possible further inspection.

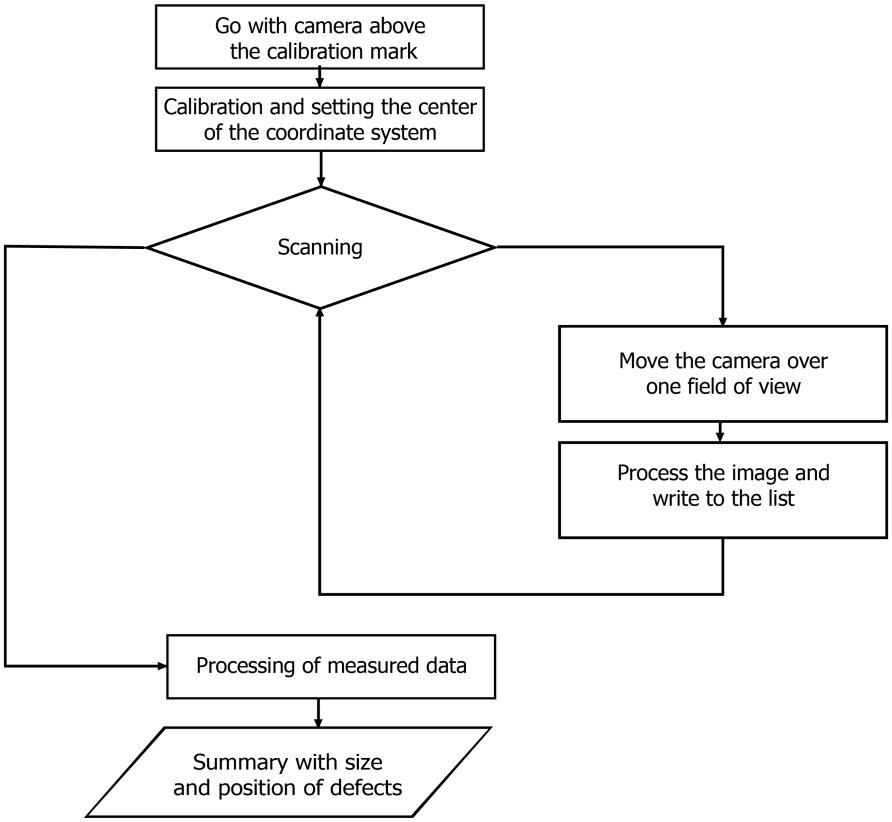

Figure 3.6: The flowchart of scanning algorithm

3.2.2. Image processing

At each camera step one an image is obtained, and it is immediately processed as large amounts of pictures are difficult to store in the random access memory. The used image process, the goal of which is to find all objects representing inappropriate defects in the image and measure their sizes and positions, is described below.

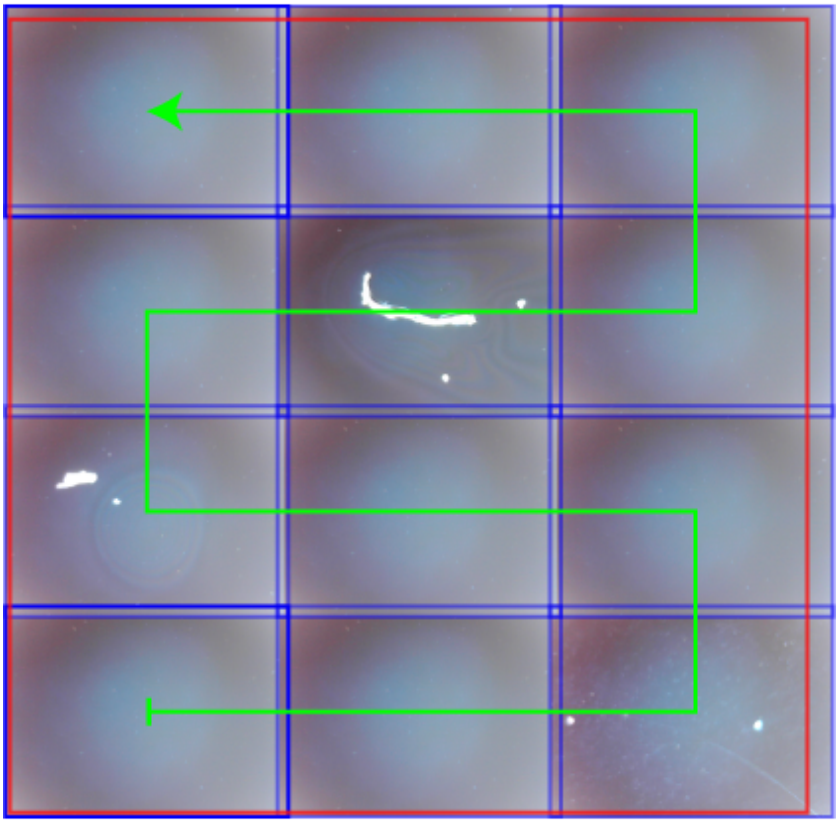

Figure 3.7: A raster scan along the zig-zag trajectory, the red square is the required area of measurement, in this case, the side is 4 mm, one image corresponds to 1.36 mm × 1.02 mm on the wafer, overlaps are approx. 0.04 mm

In the first step, an RGB image is taken and converted to a grayscale image I_G by forming a weighted sum of the R (red), G (green), and B (blue) components of the original image; the greatest weight is on G because the human eye is the most sensitive to green:

$$I_G = 0.299R + 0.587G + 0.114B \tag{3.1}$$

In the next, the image processing step of this application, some other notions will need

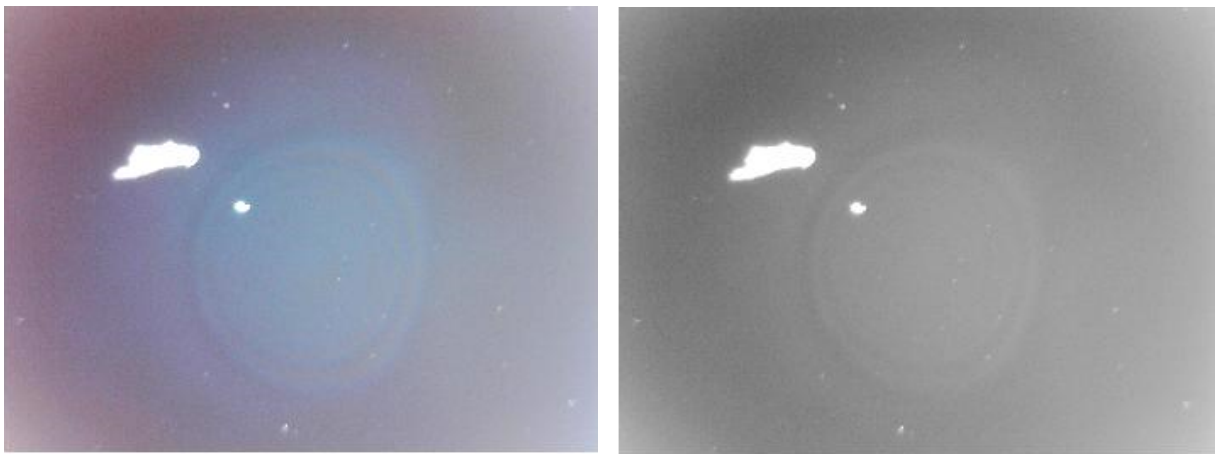

(a) RGB image (b) Grayscale image

Figure 3.8: Conversion to grayscale

to be explained. One of them is a convolution of two functions, f_1 and f_2, denoted by $f_1 * f_2$ and defined as

$$f(x,y) = \iint_{\mathbb{R}^2} f_1(s,t)\, f_2(x-s, y-t)\, ds\, dt \tag{3.2}$$

Its discrete variant in the area $\{0,1,\ldots,M-1\} \times \{0,1,\ldots,N-1\}$, useful in the image processing, is defined as

$$f(x,y) = \sum_{s=0}^{M-1} \sum_{t=0}^{N-1} f_1(s,t) f_2(x-s, y-t) \tag{3.3}$$

where f_1 is the kernel of convolution.
Very important are also the morphology operations. Basic ones are dilation and erosion. They were invented for work with binary images (containing only numbers 0 and 1). The individual methods are therefore defined by the set operators, a union $\cup$ and an intersection $\cap$. The morphology operations are applied locally – for a specific operation *a structural element* B is defined which contain values 1 and 0. It moves along the input image A while the result of the operation is saved in a reference pixel in an output image. The reference pixel changes concurrently with the structural element. If A and B are subsets of $\mathbb{Z}^2$, we note that the individual elements are not only the pixels but also the vectors, as they have a clear coordinate position with respect to [0,0]. The *reflection* of image B, denoted $\tilde{B}$, is defined as

$$\tilde{B} = \{w \,|\, w = -b, \quad for \quad b \in B\} \tag{3.4}$$

and the *translation* of set A by point $z = (z_1, z_2)$, denoted $(A)_z$, is defined as

$$(A)_z = \{c \,|\, c = a + z, \quad for \quad a \in A\} \tag{3.5}$$

the *dilation* of A by B, denoted $A \oplus B$, is given by

$$A \oplus B = \{z \,|\, (\tilde{B})_z \cap A \neq \varnothing\} \tag{3.6}$$

and the *erosion* is defined as

$$A \ominus B = \{z \,|\, (B)_z \subseteq A\} \tag{3.7}$$

These operations can be extended to a grayscale image $I_G(x)$ and a grayscale structural element $g(x)$. The formula for dilation is then given by

$$(I_G \oplus g)(x) = \sup_{y \in g} [\, I_G(y) - g(x-y) \,] \tag{3.8}$$

where sup denotes the *supremum* and the erosion is given by form 3.9, where inf denotes the *infimum*. Assume that we have a bright object on a dark background. In the case of the dilatation, the object area is enlarged and the boundary area grows. In the case of the erosion, it is reduced. If a dark object is placed on at bright background, it is in the opposite way.

$$(I_G \ominus g)(x) = \inf_{y \in g} [\, I_G(x+y) - g(y) \,] \tag{3.9}$$

Other morphology operations include *closing* and *opening*. Closing is achieved by applying the dilatation (for filling the gaps) and then the erosion. Opening works in the opposite way, first the erosion (small objects disappear) and then the dilatation [6][7][11][27].

In the second step, a background selection is made; it is necessary to remove an inhomogeneous lighting from the background. This is done by image opening using the circle structuring element with the radius of around 70 px. The result is subtracted from the original grayscale image.

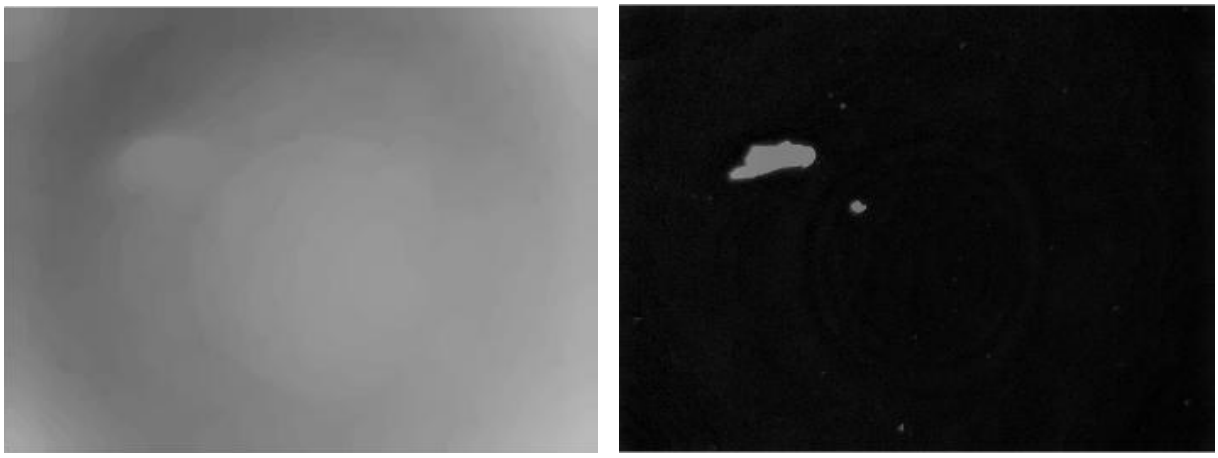

(a) The created background

(b) Difference image between the grayscale image and the background

Figure 3.9: Subtracting inhomogeneous backround

Thresholding, which is turning a grayscale image into a binary image, follows. The *treshold* is a constant t which defines the x, where the image object changes to the background. The next equation 3.10 is valid for bright objects on a dark background.

$$\begin{aligned} x \geq t &\Rightarrow \text{belongs to the object, the new pixel is equal to 1} \\ x < t &\Rightarrow \text{belongs to the background, the new pixel is equal to 0} \end{aligned} \tag{3.10}$$

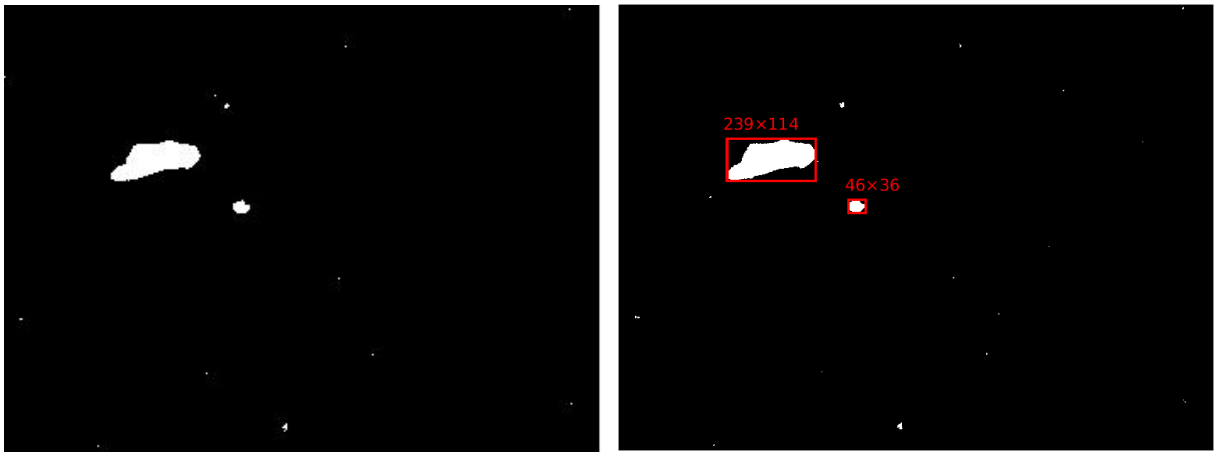

(a) Thresholded image

(b) Measurement size and position of suitable defects

Figure 3.10: Thresholding and measurement

Finally, the properties of objects in the image are measured. For this purpose, a regionprops function of Matlab Image Processing Toolbox was used, with a property 'BoundingBox'. It looks for the smallest box containing the whole object. It returns the coordinates of the minimum corner of the box and its size in pixels. If we know dimensions of the field of view and the image resolution, an obvious to convert the measured values in pixels to micrometers. Finally, the objects of defects with suitable dimensions (around 10 μm) are written to the list.

3.2.3. Locating the calibration mark

To locate the calibration mark in the image, a similar algorithm is used as in the previous subsection 3.2.2. The taken image with the calibration mark is converted to a grayscale image. Then the background is subtracted and, in this way, the created image is thresholded.

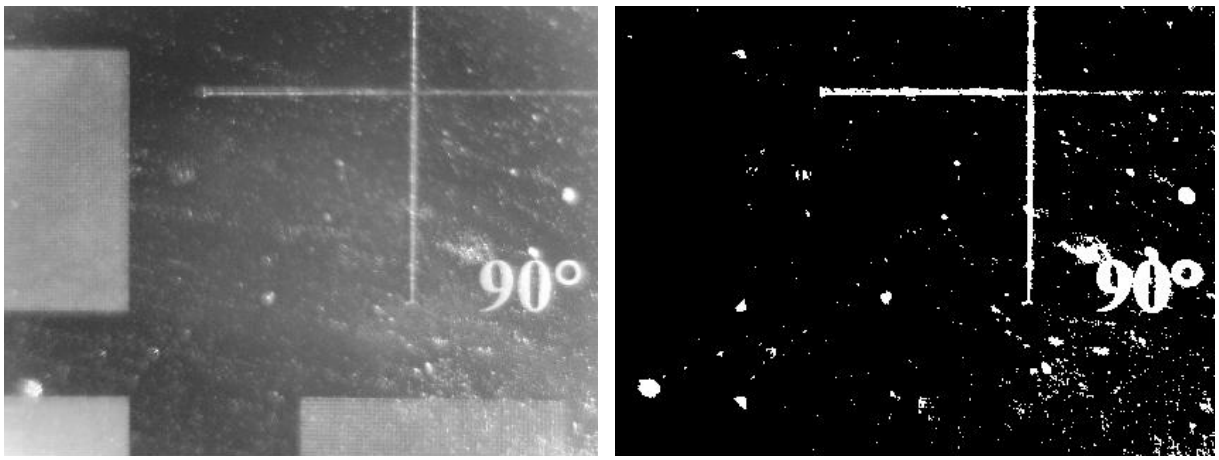

(a) Input gray-scale image (b) Thresholded image

Figure 3.11: Preparation of input image

Instead of measuring, in this case, convolution is used (formula 3.3) with the convolution matrix $\hat{f}_1$ containing a cross shape. For these purposes, the matrix with the size of 201×201 has proven the best and it is shown below.

$$\hat{f}_1 = \begin{pmatrix} 0 & \cdots & 0 & 1 & 0 & \cdots & 0 \\ \vdots & \ddots & \vdots & \vdots & \vdots & \iddots & \vdots \\ 0 & \cdots & 0 & 1 & 0 & \cdots & 0 \\ 1 & \cdots & 1 & 1 & 1 & \cdots & 1 \\ 0 & \cdots & 0 & 1 & 0 & \cdots & 0 \\ \vdots & \iddots & \vdots & \vdots & \vdots & \ddots & \vdots \\ 0 & \cdots & 0 & 1 & 0 & \cdots & 0 \end{pmatrix}$$

In this way, the central place of the cross in the picture is highlighted and the pixel with the maximum value in the image is the pixel of the center of the cross.

Subsequently, the distance from the pixel with the maximum value to the center of the field of view is calculated and converted from pixels to micrometers. Finally, the camera is moved to the new destination by given number of steps of the stepper motor.

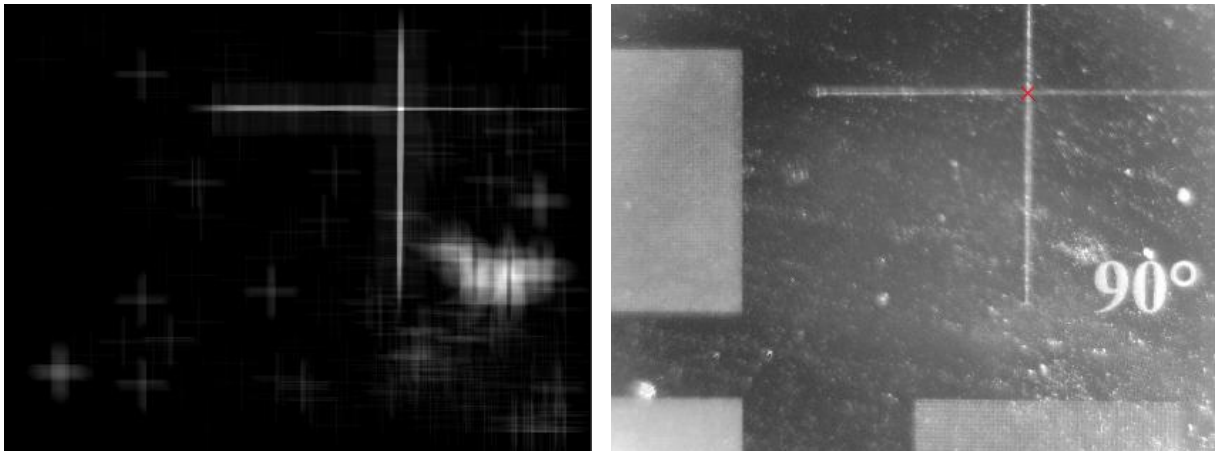

(a) Product of convolution (b) The brightest pixel was found

Figure 3.12

3.3. Measurements

For the testing measurements, a wafer inapplicable for deposition (found with a visible-light microscopy) was used. All the measurements were performed under the laminar flow in order to reduce the chance of an extra defect occurring.

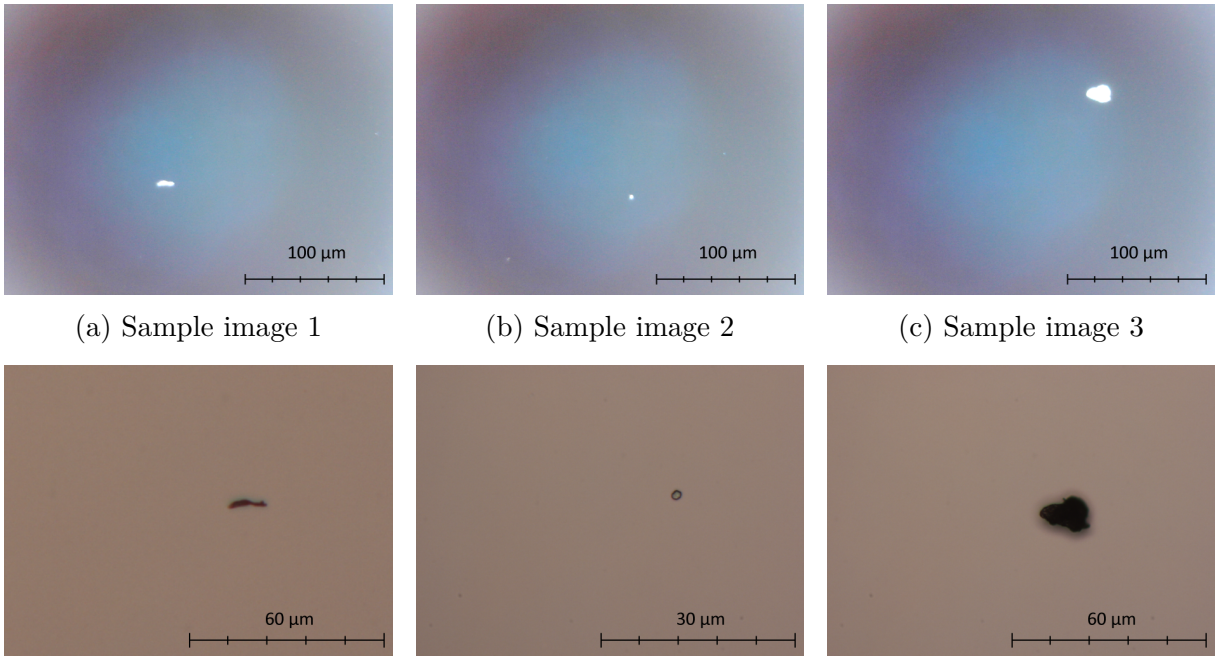

(a) Sample image 1 (b) Sample image 2 (c) Sample image 3

(d) (e) (f)

Figure 3.13: Sample images (a), (b), and (c) used in measurements and images of same defects (d), (e), and (f) taken under the visible-light microscope

For the measurements, three different images with different sized defects were chosen. Images were taken by the same camera that is used in the WaferScan. The sample image 1 (fig. 3.13a) with a thin impurity 62 µm × 14 µm, then the sample image 2 (fig. 3.13b), where there is a small hole in the resist layer with the dimensions 8 µm × 7 µm,

smaller than the size limit for the inappropriate defects. And in the last sample image 3 (Fig. 3.13c), there is a larger defect, fallen dust, with the dimensions 80 µm × 58 µm.

In the first measurement, the size of the circle structuring element is tested and used to select a background; the background is necessary to remove inhomogeneous lighting. The radius r of this element is increased by 5 px from 0 px to 150 px. And the values of position and the dimensions of each defect in the sample images are measured depending on the variable r. Relative values are used for possible comparison in one graph, they are relative to the median of given values. The median was chosen because a constant value is expected to be around the optimal value whereas a large variance is expected around the extreme values of the measured interval. Specifically, it is the value of the coordinates of the defect in the picture, $x_r = x/\tilde{x}$, and $y_r = y/\tilde{y}$ and the values of dimensions, weight $w_r = w/\tilde{w}$, and high $h_r = h/\tilde{h}$. Values x, y, w and h are measured in pixels. The measured values are plotted on a graph, always to the appropriate sample figure 1, 2, and 3., see fig. 3.14.

In graphs, there are long constant parts, which means that the radius of the structuring element does not have a big influence on the resulting values, within the required accuracy. Only defects with larger dimensions are problematic as they are interchangeable with the inhomogeneous lighting. The graph, based on the sample image 3 with the largest defect, has a large scatter to $r = 45$ px and from $r = 115$ px, consequently, the radius of the structuring element from the interval 60 px to 100 px is ideal. It will be optimal to choose the value 80 px from the center of this interval.

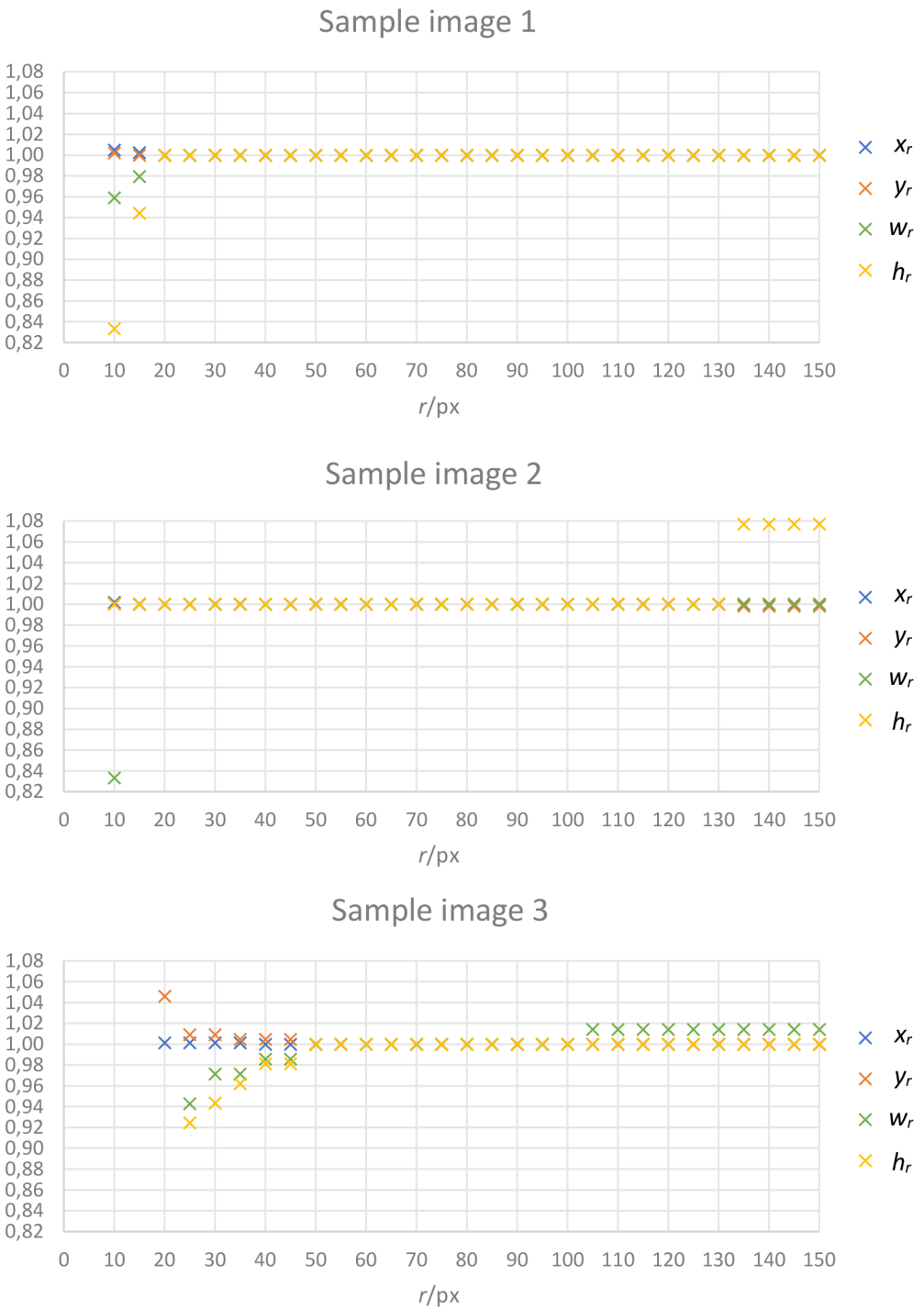

Figure 3.14: The dependence of relative properties x_r, y_r, w_r, and d_r of the defect on the radius r of the structural element

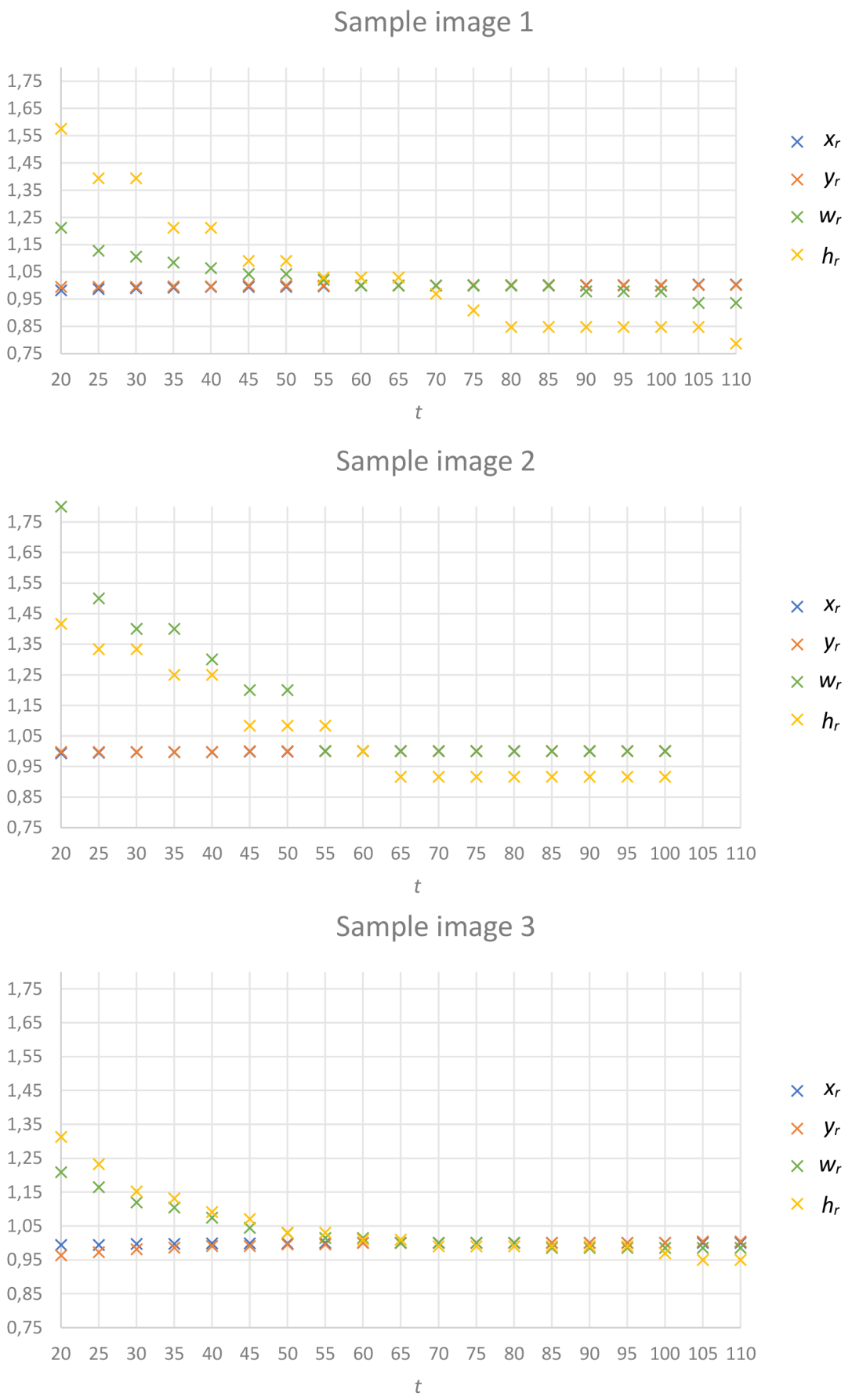

Figure 3.15: The dependence of relative properties x_r, y_r, w_r, and d_r of the defect on the threshold t

In the second measurement, the threshold constant t is tested in the same sample images as it was tested in the first measurement. The threshold is increased by 5 px from 0 px to 150 px. The radius of the structuring element from the previous measurement was set to 80 px. The measured values are plotted on a graph, see fig. 3.15.

The results are not surprising. With a lower value of t, the object of defect begins to merge with the background. Some pixels of the background are incorrectly assigned to the object; therefore, it appears larger. In the measured values, it is up to the threshold 55. With the increasing threshold value t, there appears another problem – in the case of the sample image 1 and 3, no defect was found when it exceeded the value 110; in the case of the sample image 2, the value was even 100. It can be explained as follows: in the image, there are no pixels lighter than t and only the groups of the brightest pixels represent defects. In other words, there is no lighter pixel in the image than the threshold and thus the defect, represented by a lighter pixel than the threshold, is not found. Therefore, the safe threshold value can be set somewhere within the interval 60 to 90.

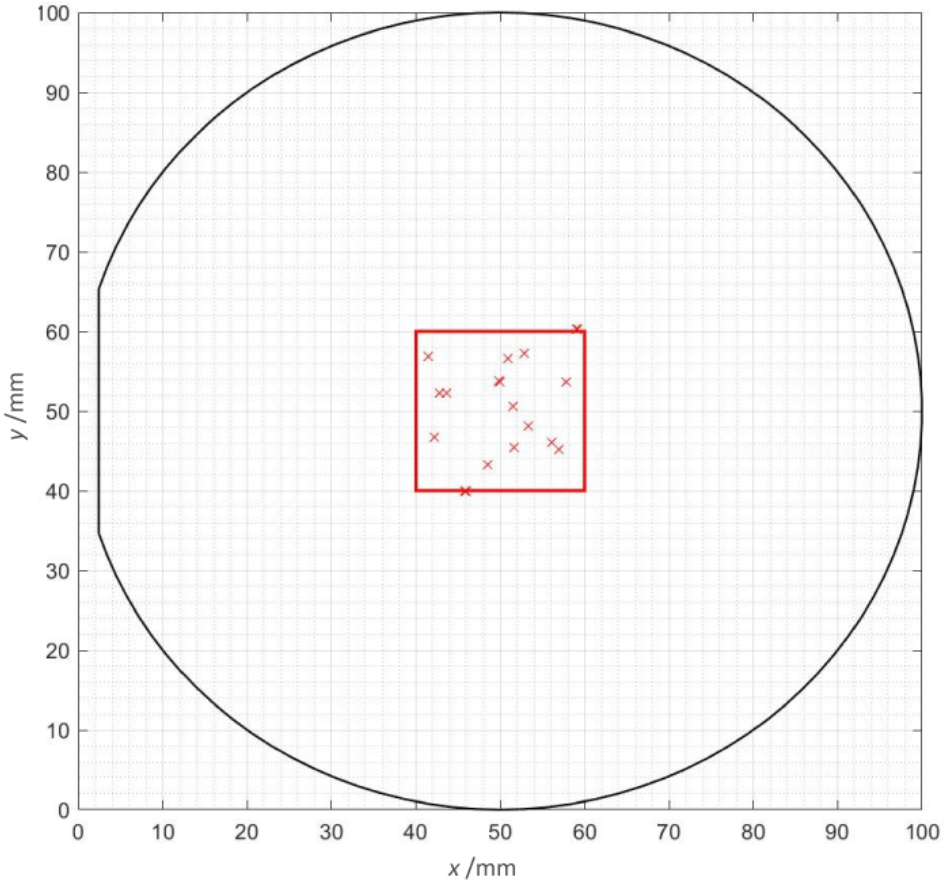

Figure 3.16: Maps of defects, detected during the last scanning (no. 10)

In last measurement, the scanning was made ten times by the WaferScan, the detection was set to defects larger then 10 µm. It took place in the scanning zone 1 cm × 1 cm in the center of the wafer. All the scans were doe immediately after each other, without any wafer manipulation. The total number of defect n, detected during the scanning, is written in the table 3.1. The defects smaller than 10 µm, and therefore incorrectly detected, were manually discarded, in terms of images taken during each scanning process. From these images, it was also clear that some of the detected defects were mere errors, they did not

constitute defects. And some of the defects were detected two times (see the sign 2x in the table 3.1).

One possible explanation of the so differing results may have to do with the fact that some impurities could occur on the resist surface during the particular measurements. The x axis of the WaferScan set up is above the wafer surface and it may cause an additional contamination with particles from the timing belt or with the lubricant of the linear guides. Also, in the border parts of the picture, it manifests a coma in which point light sources such as defects appear distorted and as such could appear several times bigger. The larger dimension of this defect is around 15 µm, which is close to the set limit of 10 µm. It then follows that this defect was smaller and should not be accepted as a defect.

Table 3.1: The number of total defects found during ten scanning processes and numbers of errors that occurred

Scanning	n	**Too small**	**2x**	**Error**	**Right**
1	20	12	0	1	7
2	23	15	1	0	7
3	24	13	3	0	8
4	23	12	2	1	8
5	23	13	2	0	8
6	24	14	2	0	8
7	26	14	2	2	8
8	26	14	2	2	8
9	22	12	2	0	8
10	21	13	0	0	8
Mean	**22.9**	**13.2**	**1.6**	**0.6**	**7.5**
Dispersion	3.3	1.0	0.8	0.6	0.7
Microscope	**5**	**0**	**0**	**0**	**5**

Thereafter, all the measured data were sorted and the properties of defects corresponding to the sample images 1, 2, and 3, and the one extra defect 4 were transferred to a separate table 3.2. The overall mean, the dispersion, the standard deviation (SD), and the coefficient of variation (CV) of the measured data were calculated. Also, the defects were found and measured with the visible-light microscope to compare the values of positiosn x, y and the dimensions $w \times h$.

The highest CV, i.e. 6 %, comes from the values of weight w. The CV of height is lower, approx. 3 %. The CV of position is up to 1 %, but there is a more useful maximal absolute error. In some cases, it is 1 mm. This kind of error could be caused by detection in an adjacent field of view, it corresponds to its size. This would explain the discrete distribution of position values in the table. It is possible that the camera has a cache and the image is read up later, one field of view away.

In a comparison to the values obtained by manual inspection using the classical visible-light microscope position, the differences are max. ±2.8 mm, which is caused by the most by inaccurate and unequal location of the wafer under the visible-light microscope and in the WaferScan set up. In the comparison of defect dimensions, mainly, the defects appear larger than they are. This is due to a high brightness of the defects. Thus, it also means that more defects than necessary will be detected. If the null hypothesis is stated as “It is

Table 3.2: Measured values of four defects during ten scanning processes by WaferScan and one manual measurement with the visible-light microscope

	Defect 1 (sample image 1)				Defect 2 (sample image 2)			
Scanning	x/**mm**	y/**mm**	w/**µm**	h/**µm**	x/**mm**	y/**mm**	w/**µm**	h/**µm**
1	43.9	57.6	64	28	41.4	56.8	15	16
2	43.9	57.6	64	28	41.4	56.9	14	17
3	43.9	57.7	64	27	41.4	56.9	15	16
4	43.9	57.7	64	26	42.7	56.9	14	17
5	42.6	57.7	64	29	42.8	56.8	14	19
6	43.9	57.6	65	27	41.4	56.9	15	16
7	43.9	57.6	64	26	41.4	56.9	14	16
8	43.9	57.6	64	30	41.4	56.9	15	18
9	43.9	57.6	63	26	41.4	56.9	15	17
10	43.9	57.6	64	27	41.4	56.9	14	16
Mean	**43.8**	**57.6**	**64**	**28**	**41.7**	**56.9**	**15**	**17**
Fispersion	0.2	0	0.1	1.2	0.3	0	0.2	0.7
SD	0.4	0	0.4	1.1	0.5	0	0.4	0.8
CV	0.01	0	0.01	0.04	0.01	0	0.03	0.05
Microscope	**43.2**	**57.0**	**62**	**14**	**43.4**	**57.2**	**8**	**7**

	Defect 3 (sample image 3)				Defect 4			
Scanning	x/**mm**	y/**mm**	w/**µm**	h/**µm**	x/**mm**	y/**mm**	w/**µm**	h/**µm**
1	58.2	45.2	95.9	71	52.8	57.3	47	44
2	56.9	45.2	91.0	70	52.7	57.3	47	46
3	56.9	45.2	91.0	70	52.8	57.3	48	43
4	58.2	45.2	89.3	69	54.1	57.3	45	48
5	58.2	45.2	90.3	71	54.1	57.3	47	48
6	58.2	45.2	90.1	71	54.1	57.3	48	45
7	56.9	45.2	89.0	68	54.1	57.3	45	48
8	56.9	45.2	85.9	66	52.8	57.3	46	43
9	56.9	45.2	91.8	62	52.8	57.3	46	40
10	56.9	45.2	89.3	69	52.8	57.3	46	43
Mean	**57.4**	**45.2**	**90**	**69**	**53.31**	**57.3**	**46**	**45**
Dispersion	0.4	0	5.7	6.7	0.4	0	0.8	7.4
SD	0.6	0	2.4	2.6	0.6	0	0.9	2.7
CV	0.01	0	0.03	0.04	0.01	0	0.02	0.06
Microscope	**59.1**	**45.3**	**80**	**58**	**54.7**	**57.5**	**32**	**29**

a defect", then the type I error means that the defect was incorrectly marked – in reality, it is not a defect. This error appears much larger than the type II error – an actual defect which is not marked as such. The type II error must approach zero, which was proved by this measurement. All the suitable defects were found; and there were even found more defects than they were seen by the visible-light microscope with a 5X lens.

3.4. Possible future solutions

Most of the problems could be solved by a better camera and optical system. The low-cost compact camera microscope (described in 3.1.2) used a lot of optical aberrations and the access to individual camera parameters is very problematic, too. A better camera should have higher resolution and its optical system should have significantly limited aberrations, especially astigmatism, field curvature, coma and distortion. And a large number of individual parameters could be set. Moreover, a system with a higher field of view, i.e. around 3 mm, could be used to reduce the number of images to scan and accelerate the measurement.

An attempt was made to solve the problem with impurities which occur on the resist surface during particular measurements by installing a housing around the x axe along which the camera moves. It is the main place from which the particles could fall on the wafer. The number of fallen particles decreased, however, some of them still appeared in the order of units. As a final and clearly effective solution seems to have both axes under the wafer surface (fig. 3.17). This was, nothing will be moving above the wafer which could cause particles to fall to the surface of the wafer.

In connection with a faster and more reliable XY movement system and a camera with a higher resolution and a superior optical system, it is possible to design a set up in the future that will be faster and more accurate. Such a set up could be used for pattern wafers or it could be used to create an image collage of the general preview of larger patterns.

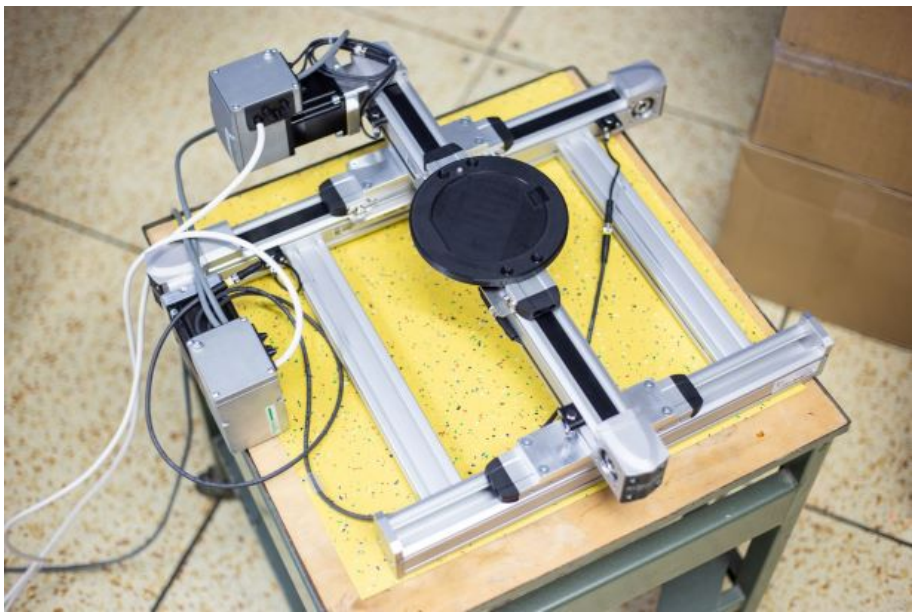

Figure 3.17: The new solution of XY movement under the wafer surface

4. Conclusions

The goal of this thesis was to design the mechanical and the electronic part of a set up intended for an inspection of resist layers coated on silicon wafers. To create an inexpensive set up that could handle work which normally takes scientists several hours to accomplish.

In the first part of this work literary research of the EBL process was done. It covered the history of EBL, the electron beam lithography system, the preparation of the resist layer, the exposition, the development of the exposed pattern as well as the inseparable part – an inspection of the resist layer prior to the electron beam exposure. Defects, which may occur in the resist were divided in two groups – defects caused by impurities and defects caused by the processing technology of spin coating and prebaking.

To facilitate an automated inspection of the resist layer a set up was designed which was adapted from the open platform of the 3D printer Prusa i3 MK2. The set up contains two stepper motors with a sufficient accuracy of movement, i.e. 20 µm per one step. Special holders were designed to hold the camera and the wafer. The wafer holder contains a calibration system to set a correct coordinate system for each measurement and an engraved rectangular square to set the squareness of individual axes to each other.

In the electronic part of the set up, the Arduino UNO® control board was used. It is the first in a series of USB Arduino boards and is thus easily connectable to a computer. It has also many extension modules that are very useful, e.g. when the motors are controlling. The camera chosen an inexpensive one, serving to eliminate and test all errors as well as the designed set up. It easily connect to a computer via USB and it has its own lighting adjustable by a potentiometer. It also has its own manual focus system, which is still used to the maximum in this application.

To synchronize the movement of the XY system and the capturing of images by the camera, the Matlab with a graphic user interface (GUIDE®) was used. A custom program was developed to create an interface for entering detection input parameters, to make raster moves with the camera along the zig-zag trajectory and to process all captured images by the developed image algorithm. The image process comprises several parts converting RGB image to a grayscale image, followed by a removal of inhomogeneous lighting from the background by image opening with a circle structuring element so as to select and subsequently subtract the background from the original grayscale image. This is followed by thresholding to separate the objects of defects from the background. Lastly, the properties of these objects are measured and written to the list of defects with all their parameters. A defect map is saved to clearly illustrate the places in the wafer appropriate for the deposition.

Finally, a set of experimental measurements was performed to evaluate the results. In the first measurement, an optimal radius of the structuring element was found by taking three sample images. The interval of radius was 60 pix to 100 pix and thus the middle of 80 pix was found as the best. In the measurement which followed, an optimal threshold was found. With a lower threshold value, the object of defect began to merge with the background and therefore some pixels of the background were incorrectly assigned to the object, so it appeared larger. With an increasing threshold value, no other pixel in the image is lighter than the value, leading to a situation where defects which do occur in the picture are not found. The optimal threshold was determined to be within the interval 60 to 90. In the final set of measurements, the repeatability and the measurement accuracy

in comparison to a visible-light microscope were tested. Generally, the defects appeared larger than they were. This is caused by a large number of optical aberrations.

The defects occurring on the resist layer during the measurement process present problems. An effective solution is to have both axes under the wafer surface. This was, there are no movable parts above the wafer which could cause particles to fall to the resist of the wafer.

Bibliography

[1] BERMUDEZ, V. M. Low-energy electron-beam effects on poly(methyl methacrylate) resist films. *Journal of Vacuum Science Technology B: Microelectronics and Nanometer Structures* [online]. 1999. Vol. 17, no. 6p. 2512-2518. [Accessed 07 June 2020]. DOI 10.1116/1.591134. Retrieved from: http://scitation.aip.org/content/avs/journal/jvstb/17/6/10.1116/1.591134

[2] FOLLAND, G. B. *Fourier analysis and its applications*. Providence : American Mathematical Society, 1992. ISBN 978-0-8218-4790-9.

[3] FRANSSILA, S. *Introduction to microfabrication*. John Wiley, 2004. ISBN 0-470-85105-8.

[4] GATZEN, Hans-Heinrich, SAILE, VOLKER and LEUTHOLD, J. *Micro and nano fabrication: tools and processes*. Heidelberg : Springer, c2015. ISBN 978-3-662-44394-1.

[5] GEMMA, Rius Suñé. *Electron beam lithography for Nanofabrication*. Doctoral thesis. Universitat Autònoma de Barcelona, 2008.

[6] GONZALEZ, Rafael C. and WOODS, Richard E. *Digital image processing*. 2nd ed. Upper Saddle River : Prentice Hall, c2002. ISBN 0201180758.

[7] HARALICK, Robert M., STERNBERG, Stanley R. and ZHUANG, Xinhua. Image Analysis Using Mathematical Morphology. *IEEE Transactions on Pattern Analysis and Machine Intelligence*. 1987. Vol. PAMI-9, no. 4p. 532-550. DOI 10.1109/TPAMI.1987.4767941.

[8] KIRCHAUER, H. *Photolithography simulation*. Wien : Österreichischer Kunst- und Kulturverlag, 2000. Dissertationen der Technischen Universität Wien. ISBN 3-85437-204-3.

[9] LALOVA, A. and TODOROV, R. Optical properties of thin PMMA films for sensor application. *Bulgarian Chemical Communications*. 2015. 47. 29-34.

[10] KNÁPEK, A., et al. Automated system for optical inspection of defects in resist coated non-patterned wafer. *Jordan Journal of Physics*. 2020. Vol. 13, no. 2.p. 93-100.

[11] KOBAN, M. *Segmentace míšního kanálu a meziobratlových plotének v MRI datech*. Bachelor Thesis. Brno University of Technology, 2018.

[12] KOEPERNIK, C. et al. Mask patterning using chemically amplified resists and the novel STEAG HamaTech Blank Coater ASR5000. In : *PROCEEDINGS VOLUME 4889* [online]. 22nd Annual BACUS Symposium on Photomask Technology : SPIE, 2002. p. 725-736. [Accessed 07 June 2020]. Retrieved from: https://www.spiedigitallibrary.org/conference-proceedings-of-spie/4889/0000/Mask-patterning-using-chemically-amplified-resists-and-the-novel-STEAG/10.1117/12.467424.short?tab=ArticleLink

[13] KOCH, Ch. and RINKE, T. J. *Photolithography: Basics of Microstructuring*. MicroChemicals, 2017. ISBN 978-3-9818782-1-9.

[14] MATEJKA, F. *Praktická elektronová litografie* [online]. Brno : Ústav přístrojové techniky AV ČR, 2013. ISBN 978-80-87441-04-6. Retrieved from: http://ebl.isi-brno.cz/

[15] MATĚJKA, M. *Technologie přípravy hlubokých struktur v submikronovém rozlišení*. Doctoral Thesis. Brno University of Technology, 2016.

[16] NISHI, Y. and DOERING, R. *Handbook of semiconductor manufacturing technology*. Second Edition. Boca Raton : CRC Press, 2007. ISBN 978-1-57444-675-3.

[17] NORRMAN, K., GHANBARI-SIAHKALI, A. and LARSEN, N. B. 6 Studies of spin-coated polymer films. *Annual Reports Section "C" (Physical Chemistry)* [online]. 2005. Vol. 101, p. 174—201. [Accessed 07 June 2020]. DOI 10.1039/b408857n. Retrieved from: http://xlink.rsc.org/?DOI=b408857n

[18] OBERAI, A. and YUAN, J-S. Smart E-Beam for Defect Identification Analysis in the Nanoscale Technology Nodes: Technical Perspectives. *Electronics, MDPI* [online]. 2017. No. 6, 87. [Accessed 08 June 2020]. Retrieved from: https://doi.org/10.3390/electronics6040087

[19] OKAZAKI, Shinji. Resolution limits of optical lithography. *Journal of Vacuum Science Technology B: Microelectronics and Nanometer Structures*. 1991. Vol. 9, no. 6. DOI 10.1116/1.585650.

[20] PÁNEK, P., LÍBEZNÝ, M., LORENC, M., ŠIK, J., VÁLEK, L., PLACHKÝ, T., ULRYCH, J., ŠPETÍK, Z., ŠPETÍK, R., HOLÍK, Š. and DOROTÍK, M. *Základy technologie výroby polovodičů*. Brno : CERM, 2016. ISBN 978-80-7204-939-4.

[21] PETERSON, I., et. al. Lithography Defects: Reducing and Managing Yield Killers through Photo Cell Monitoring. *YMS Magazine* [online]. Vol. 2000, no. Springp. 17-24. [Accessed 07 June 2020]. Retrieved from: https://www.ymsmagazine.com/wp-content/uploads/magazine_summer00_coverstorysu00.pdf

[22] RAI-CHOUDHURY, P. *Handbook of microlithography, micromachining, and microfabrication*. London, UK : Institution of Electrical Engineers, c1997. IEE materials devices series, 12A-12B. ISBN 0819423793.

[23] RIZVI, Syed (ed.). *Handbook of Photomask Manufacturing Technology*. Boca Raton : CRC Press, 2005. ISBN 9781315220833.

[24] SENEFELDER, A. *A Complete Course of Lithography*. London, R. Ackermann, 1819.

[25] ŠAMOŘIL, T. *Aplikace fokusovaného iontového a elektronového svazku v nanotechnologiích*. Doctoral Thesis. Brno University of Technology, 2015.

[26] THOMPSON, L. F., WILLSON, C. G. and BOWDEN, M. J. (eds.). *Introduction to Microlithography*. Washington, D. C: American Chemical Society, c1983. ACS Symposium Series. ISBN 0-8412-0775-5.

[27] YOUNG, I. T., GERBRANDS, J. J. and VAN VLIET, L. J. *Fundamentals of image processing*. Version 2.2. Delft University of Technology, 1998. ISBN 90-75691-01-7.

5. List of Symbols, Physical Constants and Abbreviations

C	polymer concentration
CV	coefficient of variation
η	intrinsic viscosity
D	electron beam dose
D^i	dose of complete exposure
D^o	dose that causes no resist dissolution
DOVID	diffractive optically variable image device
EBL	electron beam lithography
γ	contrast
ISI CAS	Institute of scientific instruments of the Czech Academy of Science
J	current density
λ	wavelength
MTF	modulation transfer function
NA	numerical aperture
$\hat{\omega}$	convolution matrix
p	spatial period
PMMA	polymer polymethyl methacrylate
R	optical resolution
SD	standard deviation
SEM	scanning electron microscope
t	thickness of resist layer
τ	time of the exposure of one dose

6. List of Appendices

A. Program code example

B. A detailed picture of the automated set-up

C. Article: Automated system for optical inspection of defects in a resist coated non-patterned wafer

A. Program code example

The sample is from the main function of the program, with which image analysis is performed:

```
global xpix;    %the resolution of the camera in the x axis
global ypix;    %the resolution of the camera in the y axis
global xstep;   %the number of motor steps per displacement of the one field of view in the x axis
global ystep;   %number of motor steps per displacement of the one field of view in the y axis
global index;   %an index of pictures which contains the defects
global list;    %the list of detected defects
global destination; %destination where to save the image
global cam;     %camera setting

xmicrons=1360;  %dimensions of the field of view in µm
ymicrons=1020;
bgconst=80; %radius of the circle structuring element, used in background selection
bin = 75;   %treshold
limit = 10; %the limit of the size of the defect, in µm
limit = ceil(limit*xpix/xmicrons);  %transfer the limit to pixels
capture = 0;

img = snapshot(cam);    %load the image from the camera
gray = rgb2gray(img);   %RGB to grayscale conversion
background = imopen(gray,strel('disk',bgkonst));    %image opening with the circle structuring element to create background
fine = gray-background; %subtraction of background from original grayscale image
bi=fine>bin;    %thresholding

%the defects detection:
boxes = regionprops(bi,'BoundingBox'); %Measure properties of image regions by rectangles
    rectangles = [boxes.BoundingBox];   %trasfer them to array

for i = 1:(size(rectangles,2)/4)
  if (rectangles(4*i-1)>=limit)&&(rectangles(4*i)>=limit)  %discard small defects
    capture=1;  %the image will save, the images where defect was not found are not saved
    %transfer properties from pix to µm and write them to the list:
        x = (xstep)/50+((rectangles(4*i-3)-xpix/2)*xmicrons/xpix/1000);
        y = (ystep)/50+((ypix/2-rectangles(4*i-2))*ymicrons/ypix/1000);
        dx = rectangles(4*i-1)*xmicrons/xpix;
        dy = rectangles(4*i)*ymicrons/ypix;
        list = cat(1,list,[index,xstep,ystep,rectangles((4*i-3):(4*i)),
        round(x,1), round(y,1),dx,dy);
  end
end
if capture == 1 %save the image, where the defects were found
    imwrite(img,fullfile(handles.destination,index),'jpg');
    index = index+1;  %set index to the next image
end
```

B. A detailed picture of the automated set-up

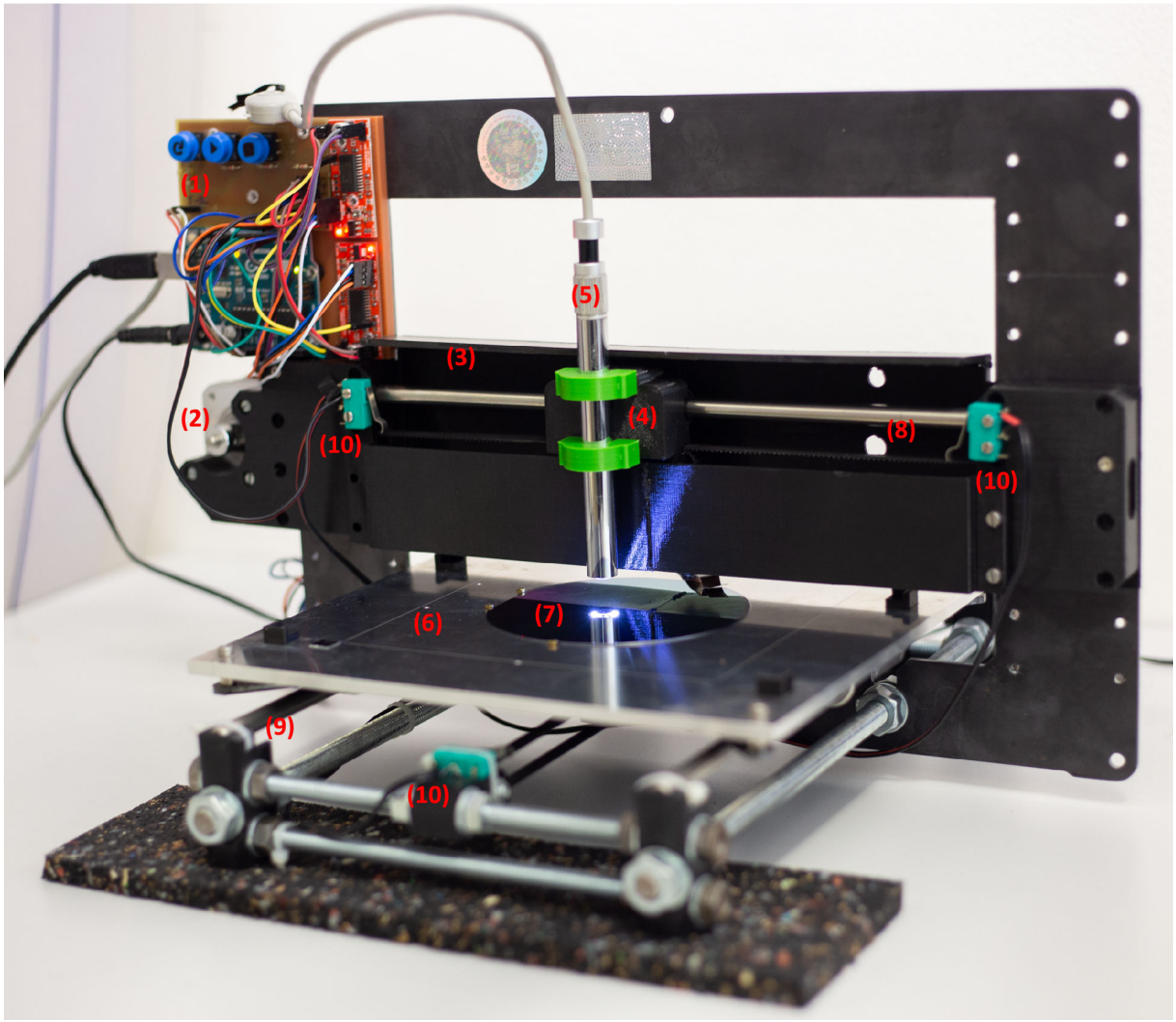

Figure B.1: (1) Electronics of the measurement set-up, (2) one of the stepper motors, (3) housing to hold back the defects, (4) camera holder, (5) camera, (6) wafer holder, (7) wafer, (8) x-axis, (9) y-axis, and (10) limit switches

C. Article: Automated system for optical inspection of defects in a resist coated non-patterned wafer

Volume 13, Number 2, 2020. pp. 93-100

Jordan Journal of Physics

ARTICLE

Automated System for Optical Inspection of Defects in Resist-coated Non-patterned Wafer

A. Knápek, M. Drozd, M. Matějka, J. Chlumská, S. Král and **V. Kolařík**

Institute of Scientific Instruments of the Czech Academy of Science, Královopolská 147, 612 64 Brno, Czech Republic.

Received on: 08/08/2019; *Accepted on: 9/2/2020*

Abstract: Quality control of the resist coating on a silicon wafer is one of the major tasks prior to the exposition of patterns into the resist layer. Thus, the ability to inspect and identify the physical defect in the resist layer plays an important role. The absence of any unwanted defect in resist is an ultimate requirement for preparation of precise and functional micro- or nano-patterned surfaces. Currently used wafer inspection systems are mostly utilized in semiconductor or microelectronic industry to inspect non-patterned or patterned wafers (integrated circuits, photomasks, … etc.) in order to achieve high yield production. Typically, they are based on acoustic micro-imaging, optical imaging or electron microscopy. This paper presents the design of a custom optical-based inspection device for small batch lithography production that allows scanning a wafer surface with an optical camera and by analyzing the captured images to determine the coordinates (X, Y), the size and the type of the defects in the resist layer. In addition, software responsible for driving the scanning device and for advanced image processing is presented.
Keywords: Optical inspection, Resist layer, Non-patterned wafer, Quality control.

Introduction

Silicon wafer is a typical substrate that is used in lithography process for microfabrication of various types of devices. The quality of the silicon wafer determines the quality of a lithographic process, just as the quality of the resist-coated surface prior to the lithography step is very important in terms of the final functionality of the fabricated micro-device. Several papers have been published reporting optical properties of polymethyl methacrylate (PMMA) films [1, 2, 3].

Generally, there are two categories of wafer inspection methods: non-patterned and patterned [4, 5]. Non-patterned wafer inspection typically investigates defects on the unprocessed silicon wafer. On the other hand, patterned wafer inspection is used for wafer control after the lithography process.

Industrial inspection devices used in semiconductor and chip manufacturing are based on two main technologies: optical and electron-beam [6, 7]. The optical inspection device typically uses laser, deep ultraviolet (DUV) or a broadband plasma light source to illuminate the wafer and acquire an optical image in the bright field or the dark field. In general, a principle of function, where a reflected laser beam carries information about a position, is illustrated in Fig. 1. The e-beam based inspection uses highly specified and automatized scanning electron microscopes that are typically used only for detailed inspection of patterned wafers [6].

Corresponding Author: Alexandr Knápek **Email**: knapek@isibrno.cz

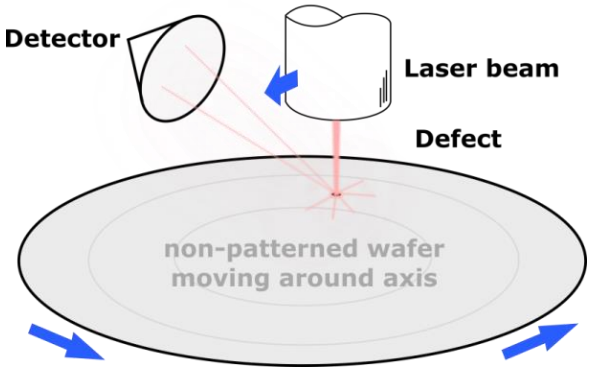

FIG. 1. Optically-based principle of defect inspection on a non-patterned wafer.

The devised approach is based on a motivation to develop an optical-based semi-automatic wafer inspection device that allows the inspection of a non-patterned [6] resist-coated wafer and would replace the current visual inspection of a wafer within the visible light microscope (VLM). Our primary aim is to find the position, the size and the type of the random defect at the layer of electron resist. That sort of evaluation is applied to a wafer surface by spin coating technique prior to its patterning by electron beam lithography (EBL).

Various types of defects are involved during the deposition of resist by spin-coating: dust contamination, micro-bubbles, bumps, craters, comets, thickness inhomogeneity … etc. [9, 10]. For the software, it is important to be able to identify not just the position of defects on the wafer, but also to estimate the type of defect, that may be considered as an essential feature, because not every type of defect can be equally problematic in the follow-up lithography process [9]. For example, a larger dust particle in or on the resist might cause a charging phenomenon, when the electron beam irradiates neighboring particles. Therefore, a charged dust particle can deflect the electron beam and reduce the dose received under and in the vicinity of the particle [11], as illustrated in Fig. 2.

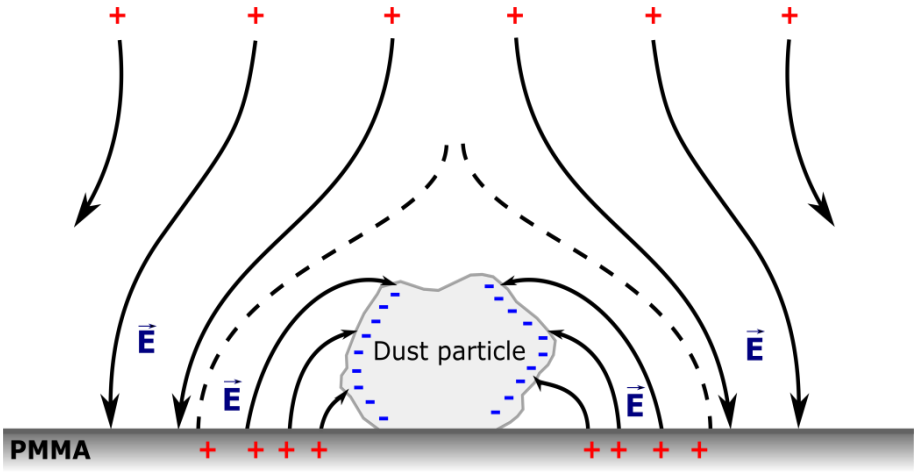

FIG. 2. Schematic of charging of a dust particle and the resulting defect in the EBL patterned wafer, with permission from Hitachi, Ltd., Tokyo, Japan [8].

It is critical to avoid patterning in the areas with particle contamination. Air bubbles might create holes in the resist after development. Comets can cause resist thickness inhomogeneity and thus an inadequate development of the recorded pattern.

Defect Analysis

The preparation of PMMA resist layers on silicon wafers by spin-coating method is performed under laminar flow in order to lower the chance of a defect occurring in the prepared layer. The PMMA and xylene solvent are mixed together and, according to viscosity, are filtered through syringe filters (the porosity level is 0.45 μm or 5 μm). Subsequently, the resist is poured

onto the silicon wafer which in this case forms an approx. 2.5μm thick compact layer.

A variety of problems may occur during the coating process. In general, the above defects can be caused by impurities on the silicon wafer, such as dust particles, impurities or micro-bubbles in the resist mixture or by e.g. poor centering of the wafer on a spin coater. The parameters considered within the process of spin coating include rotation speed, acceleration, time and the application method of the liquid resist precursor.

The first class of defects is caused by impurities that stick to the resist layer during the deposition or during the baking process, as illustrated in Fig. 3. If a dust particle or fiber falls on the wafer during deposition, it becomes coated in the resist and forms a "comet" (a small thickness difference formed from the center of the particle to the edge of the wafer). Other possible particles are small resist flakes (i.e., dried resist) that stick to the layer and become permanently attached to the surface due to the baking process.

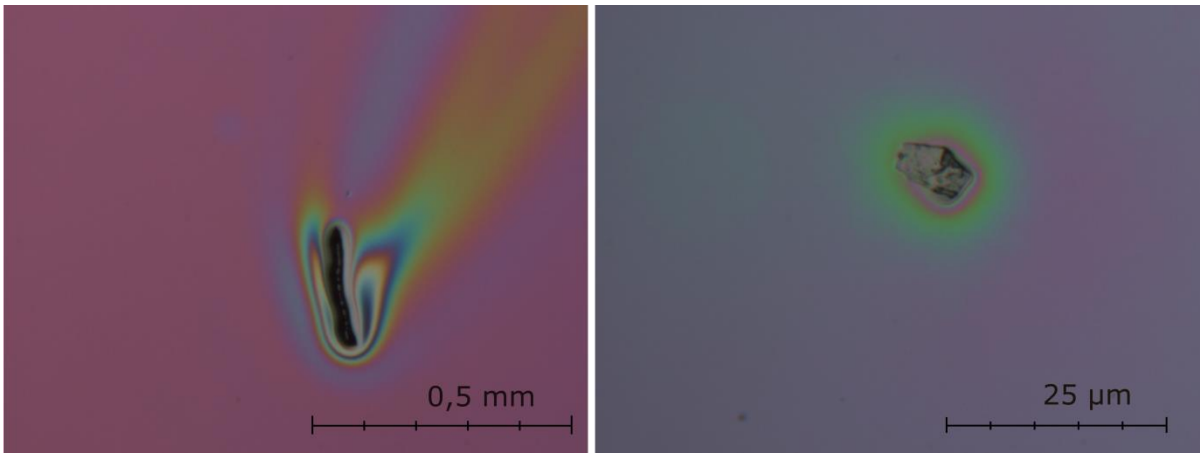

FIG. 3. Fiber creating a comet (left); a resist flake baked into the layer (right).

The second class of defects illustrated in Fig. 4 may occur randomly based on the processing technology. During the process of mixing of the resist and the solvent, air bubbles can form in the mixture. If a bubble is transferred on the wafer, it may form a defect called "micro-bubble". It is a small spot (spherical shape) in the resist layer, where there is a huge thickness difference. It may cause problems during development (for example cracks in the resist layer around the spot). It can be prevented by degassing the mixture in the desiccator or really slow pouring of the resist mixture on the wafer. Another issue that may occur is related to inhomogeneity on a much bigger scale. For example, interference circles can be seen all over the wafer. The thickness difference is formed on a bigger surface than in the case of micro-bubble defect. The exposed structure has afterwards different depths according to the location on the wafer. This type of defect can be caused by poor centering of the wafer on a spin coater, by an insufficiently levelled spin coater or by improper choice of the spin-coating parameters, as mentioned above. This type of defect cannot be seen using a microscope because of the small field of view. It can, however, be seen by the naked eye. Despite this kind of defect cannot be observed by the set-up, it has to be dealt with before the process of electron beam lithography and defected areas have to be avoided. This particular type of defect is further explained in the following paragraphs.

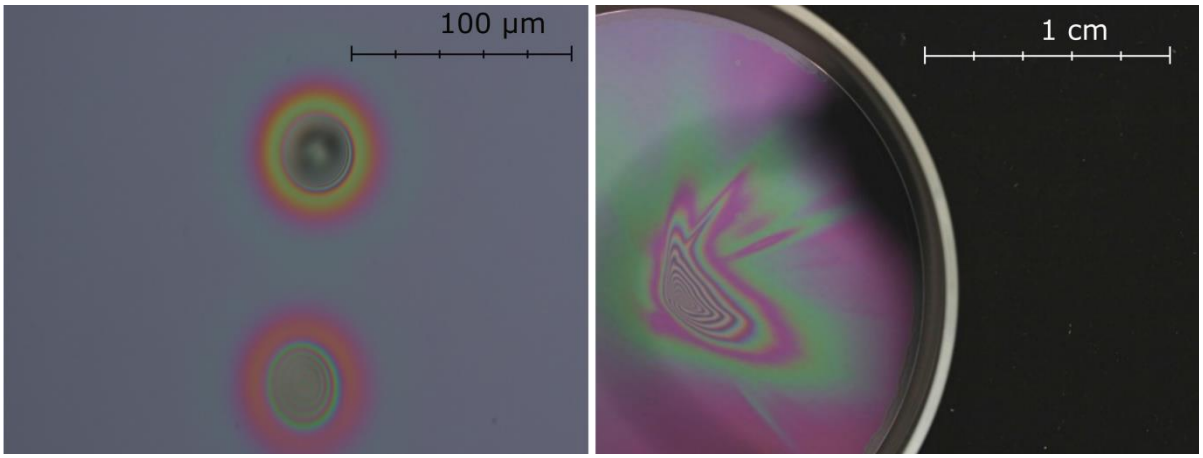

FIG. 4. Micro bubble (left), inhomogeneity all over the wafer (right). The left image was taken by VLM and the right one by a camera.

The interference effects, which can be seen in Figs. 3 and 4, are determined by the optical path length (OPL) through the thin PMMA film in a phenomenon called thin-film interference. Optical path length is the product of the geometric length *d* of the path of light through a system and the index of refraction *n* of the medium through which the light propagates, hence OPL = *nd*. Through this concept, a phase of the light can be determined by governing interference and diffraction of light as it propagates.

Recently, as was reported by Lalova [2], refractive index *n*, extinction coefficient *k* and thickness *d* of the spin-coated PMMA films deposited on a silicon wafer were determined by using minimization of a function. The function consists of the discrepancies between measured and calculated *R* spectra by means of multi-wavelength nonlinear curve fitting. The refractive index was described using Sellmeier's equation in the following form:

$$n^2(\lambda) = 1 + \frac{A_1\lambda^2}{\lambda^2 - A_2^2}, \quad (1)$$

where A_1 and A_2 are the Sellmeier's coefficients. The dispersion of the extinction coefficient was described using the following exponential dependence [2]:

$$k = B_1 \exp\left(B_2/\lambda\right), \quad (2)$$

where B_1 and B_2 are dispersion coefficients. Based on Eqs. (1) and (2), it has been found out that the refractive index of the thin PMMA increases with the increase of the thickness following an exponential law of the type $n = n_0 + A_1 (1 - \exp(-d/d_1))$, where n_0 is the initial value of the refractive index and A_1 = -0.9 and d_1 = 31.91 are parameters.

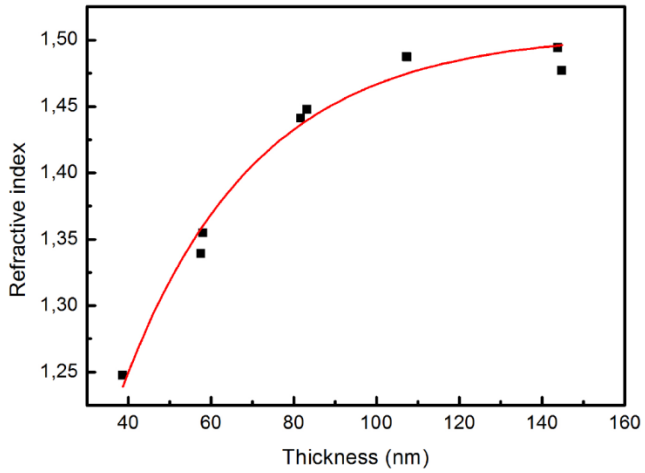

FIG. 5. Dependence of the refractive index on the thickness of thin spin-coated PMMA films at a wavelength of 600 nm, with permission from *Bulgarian Chemical Communications* [2].

Based on the dependence illustrated in Fig. 5, it has been concluded that the refractive index is thickness-dependent for values of $d < 110$ nm. For thin films with thicknesses greater than 110 nm, the coating possess refractive index is close to that of the bulk [2].

Measurement Set-Up

The measurement set-up illustrated in Fig. 6 consists of a table moving along the axis Y and a camera placed above the table which moves along the axis X. The camera is based on a classical color CMOS sensor working at a resolution of 1.3 megapixels, allowing obtaining 15 screens per second with a resolution of 1280 x 1024 pixels over the USB 2.0 bus. The camera provides also a white LED lighting, whose intensity can be controlled manually. In order to reduce a distortion caused by the lens that may appear near the edges of the image, only the inner part of the image (approx. 70% of the original image) is used and further processed.

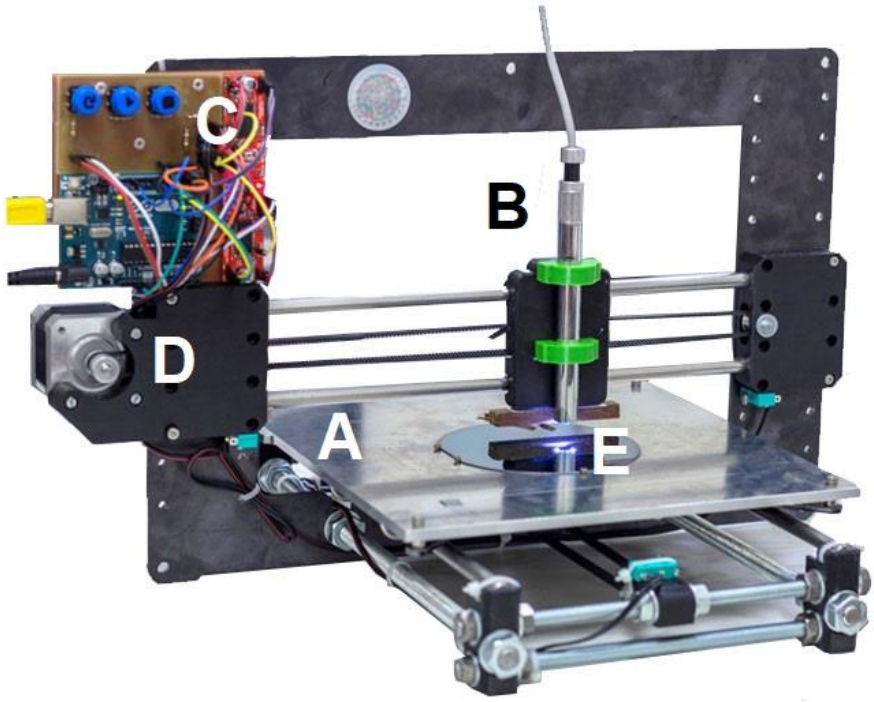

FIG. 6. Prototype of the measurement set-up scanning over a 4-inch wafer showing all the electronic and mechanical parts: (A) moving table, (B) camera on a moving holder, (C) Arduino board with buttons and stepper motor drivers, (D) stepper motor drive and (E) the evaluated 4-inch wafer.

The mechanical system was originally adapted from a 3D-printer-based platform with two precise stepper motors (see Figs. 6 and 7). The XY movement is based on the two stepper motors controlled through a microcontroller board Arduino UNO® based on the Microchip ATmega328P. The Arduino board contains its own program responsible for interpreting received commands from the WaferScan software (illustrated in Fig. 8, left), which includes driving of the movements. The board also generates a response when limit switches have reached the end of the track in one of the axes. The power supply to the motors is provided through two Easy Driver expansion boards. The whole system is powered using an external 12V DC power supply.

The main algorithm consists of a few simple steps that are implemented within an algorithm, whose flowchart is illustrated in Fig. 8 (right). In the beginning, the position of a calibration mark is located. The calibration mark is situated on a calibration sample, which is a silicon chip (1 cm^2) with a cross-structure etched into the surface. This sample is placed on the stage table that contains also the evaluated wafer. After the position of the mark is read, a new coordinate system is set. This system of coordinates is then used for determining positions of any defect found during the scanning over the surface of the evaluated wafer. The

flowchart illustrated in Fig. 8 (right) of the main scanning algorithm is implemented using Matlab graphic user interface (GUIDE®) and Matlab Instrumentation toolbox®. Matlab instrumentation toolbox provides software means to communicate with all the components directly from the software by using text-based Standard Commands for Programmable Instruments (SCPI) command or *via* instrument drivers. The process follows a simple line scanning procedure, as it is known from any other scanning devices, which means that when an image is obtained, the camera moves to another field of view until the whole surface is mapped. The implementation of post-processing uses advanced image processing and recognition techniques, whose description is outside of the scope of this paper; so, let us just simply conclude that the software returns precise coordinates and sizes of the defects found in the taken images.

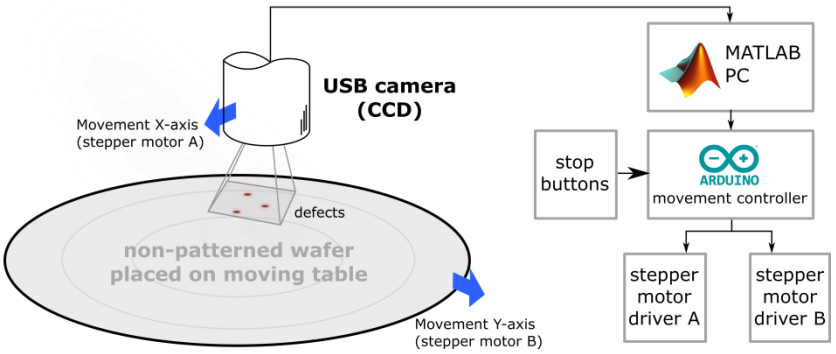

FIG. 7. Schematic illustration of the measurement set-up.

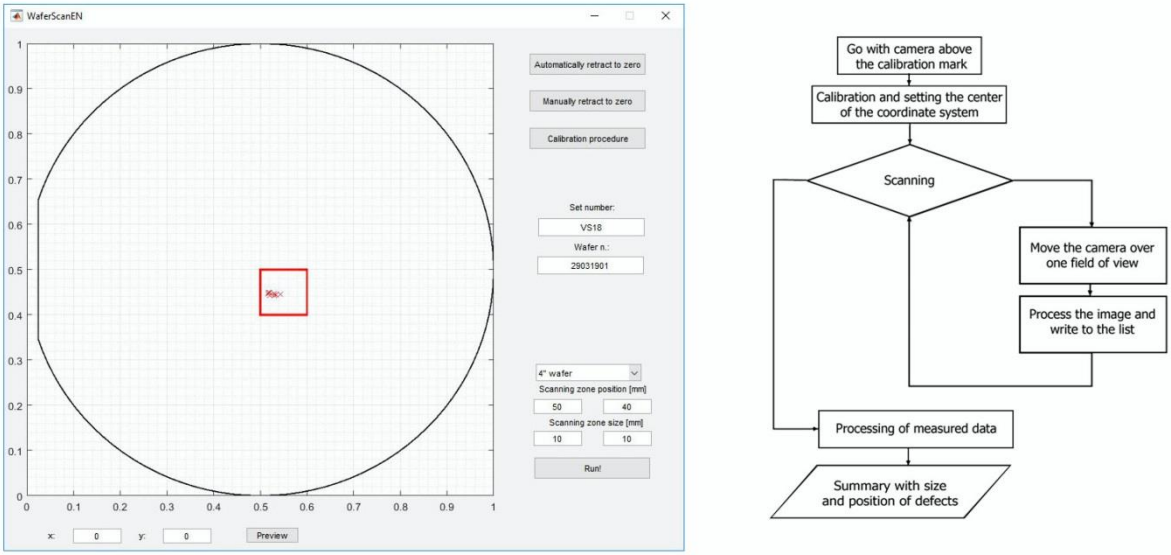

FIG. 8. The screen of the WaferScan software showing located defects in the red box (left); the flowchart of scanning algorithm schematically showing the implemented scanning procedure (right).

The WaferScan software (Fig. 8 left) allows running the initial calibration procedure both manually and automatically as well as precisely determining the area on the wafer to be scanned. On the background, the software saves a list of defects and their parameters as well as the particular images that are continually obtained for a possible further inspection. Using the saved images, it is possible to determine the size of the located defects.

Results and Discussion

A comparison of two particular defects found is illustrated in Fig. 9, showing the output of our WaferScan system compared to the images obtained by manual inspection using a classical visible-light microscope. The map of defects shows the precise positions of the particular defects found.

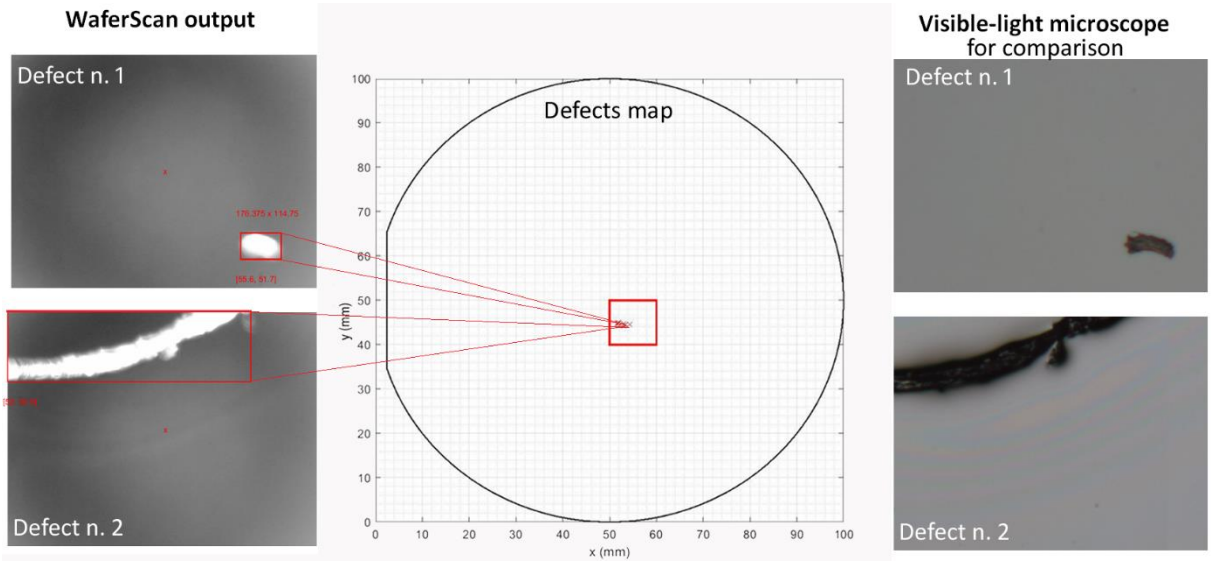

FIG. 9. Results provided for two selected defects (left top and above) within the scanning area (that is located within the red borders). On the right side, there are images from a visible-light microscope.

Summary and Conclusions

This paper presents an important tool that has been developed to cover certain needs of complex research, which are connected with the development of large-sized micro-structure diffractive optical elements as well as sub-micron diffractive holography structures for industrial holography applications.

The devised set-up enables to scan a non-patterned wafer stepwise and to find defects as small as 10 μm by means of a precise CCD camera that scans the surface. Software, that is an essential part of the device, allows determining the size of a defect and its position on the wafer. This is the most significant benefit of this set-up, since the evaluation of a small series was in most cases done manually. Moreover, the accuracy of the process was increased and its error rate was decreased.

Further development will focus on precise characterization of particular defect types and automated distinction between defects, such as micro-bubbles, fiber or dust, in addition to revealing inhomogeneities of the resist layer on a smaller scale. The set-up will be further extended by addition of an automated focusing system that would make the process more precise. Among the other future goals, the set-up may be also extended to be used for patterned wafers and to implement White Light Reflectance Spectroscopy (WLRS).

Acknowledgements

The research was supported by the Ministry of Industry and Trade of the Czech Republic, MPO-TRIO project FV10618. The research infrastructure was funded by the Czech Academy of Sciences (project RVO: 68081731).

References

[1] Norrman, K., Ghanbari-Siahkali, A. and Larsen, N.B., Annual Reports Section "C" (Physical Chemistry), 101 (2005) 174.

[2] Lalova, A. and Todorov, R., Bulgarian Chemical Communications, 47 (2015) 29.

[3] Hussein, A.S., Shinen, M.H. and Abdali, M.S., Journal of University of Babylon for Pure and Applied Sciences, 27 (4) (2019) 169.

[4] Franssila, S., "Introduction to Micro-fabrication", (John Wiley & Sons, Ltd., 2006), pp.1-15 s. ISBN 0-470-85105-8.

[5] Lapedus, M. "Inspecting Unpatterned Wafers", Semiconductor engineering, [online], 16 August 2018, Available at: https://semiengineering.com/inspecting-unpatterned-wafers/

[6] Oberai, A. and Yuan, J.-S., Electronics, 6 (2017) 87.

[7] Lapedus, M., "E-Beam *vs*. Optical Inspection", Semiconductor engineering [online], 16 July 2016, Available at: https://semiengineering.com/e-beam-vs-optical-inspection/

[8] Yoda, H. et al., IEEE Transactions on Pattern Analysis and Machine Intelligence, 10 (1) (1988) 4.

[9] Peerson, I., Thompson, G., DiBiase, T., Ashkenaz, S. and Pinto, R.H., Yield Management Solutions, 2 (3) (2000) 17.

[10] Koch, Ch., Rinke, T.J., "Photolitography: Basic of Microstructuring", 1st Ed., (MicroChemicals, GmbH, 2017), pp.58-62 s. ISBN 978-3-9818782-1-9.